COMPARATIVE ANALYSIS OF SIMULATED AND EXPERIMENTALLY FABRICATED SELF-WRITTEN WAVEGUIDES

Master Thesis written by:

Murat Baran

Hannover Centre for Optical Technologies
Leibniz Universität Hannover

First Examiner: Prof. Dr. Bernhard Wilhelm Roth
Second Examiner: Prof. Dr. Wolfgang Kowalsky
Supervisor: Dr. Axel Günther

APRIL 2021

STATEMENT OF AUTHORSHIP

I hereby declare that this thesis is written by myself. It is submitted for the master's degree in Optical Technologies at Mechanical Engineering Faculty at Leibniz University Hannover. The submitted work has not been shared anywhere else. The content of the electronic copy is the same as that of the printed copy and it is not used any sources other than those given.

Hannover, Apr. 15, 2021 Signature.........................

ACKNOWLEDGEMENTS

I would like to thank my advisors Prof. Dr. Bernhard Wilhelm Roth and Dr. Axel Günther for their mentorships, supports and helps. Their extensive and intensive knowledges and precisions in science and research consistently whenever I needed, providing me a warm working atmosphere and kindness in life deeply impressed me, and I believe that I will benefit greatly from this experience in my future endeavors.

Finally, I would like to thank to my wife, my children, and my parents for their love, support and encouragement. They are there for me whenever I needed them the most.

ABSTRACT

In the last decades, the optical adhesives have become highly promising due to their widespread applications in the numerous optical fields. There are outnumbered research studies about them and their numerous fields of application. One of these promising applications is the usage of self-written waveguides (SWW) which enable a rigid and low-loss connection between two optical components. Nevertheless, there are not enough research studies about the temperature dependency of the optical transmission through the SWW that is inspected in this study. This master's project is devoted to study the transmission of a laser beam by temperature through SWW created in the NOA 68 photopolymer medium. To verify the data from the experiment, a model is designed, simulated using the Multiphysics optical simulation software (COMSOL), and then, the simulation results are compared with the experimental data. Furthermore, the research studies do not propose anything for the durations of the internal- and external curing where the waveguide is attenuated highest that makes it very vital for the waveguide formation. This study removed the blurriness in the curing times and guide the scientists in establishing an efficient waveguide made out of NOAs.

To achieve this goal, a thermal simulation of the waveguide is made, an SWW is formed, and the experimental results of the power output, and the refractive-index profile of the waveguide are analyzed. Then, the RIs of the SWW and its cladding are measured in the refractive-index profilometer and the results are used to make the simulation in the software.

TABLE OF CONTENTS

LIST OF ABBREVIATIONS

SWW	Self-written waveguide
RI	Refractive index
NOA	Norland optical adhesive
TOC	Thermo-optic coefficient
RIPM	Refractive index profilometer
RIP	Refracted-index profile
LISW	Light-induced self-written waveguide
TIR	Total internal reflection
GRIN	Graded-index
SMF	Single-mode fiber
MMF	Multi-Mode fiber
NA	Numerical aperture
M	Number of modes
TE	Transverse electric
CTE	Coefficient of thermal expansion
PMMA	Poly (methyl methacrylate)
RNF	Refracted Near-Field Method
IML	Index matching liquid
EM	Electro-magnetic
BPM	Beam Propagation Method
TM	Transverse magnetic
WKB	Wantzel-Kramers-Brillouin
SVEA	Slowly varying envelope approximation
FEM	Finite Element Method
FEA	Finite element analysis
PDE	Partial differential equation
EWBE	Electromagnetic Waves, Beam Envelope
PO	Poweroutput

PM	Power meter
INC	Internal curing
EXC	External curing

LIST OF TABLES

LIST OF FIGURES

Chapter 1: Introduction

Self-written waveguides (SWWs) are waveguide-like optical channels formed as response of the photosensitive materials to the beam at a certain wavelength where a local photopolymerization process starts and a permanent change of the refractive index (RI) is generated which is correlated to the light intensity. It occurs when the induced RI change reaches to a sufficient value where the light is trapped along the propagation axis. In our experiment, the SWWs were formed by using Norland optical adhesive (NOA) as photopolymer medium.

Different types of optical adhesives have been attracted intensive attention in the last decades due to their widespread applications in the numerous optical fields such as manufacturing of sensors for temperature [1, 2], RI [3, 4], strain [5, 6], etc. measurement, lasers [7], coupling structures for fiber-to-fiber and fiber-to-optical device systems [8], holographic data storage [9], biologically inspired microstructures [10] etc. The temperature change in a material or an optical device affects a lot of parameters such as optical loss, RI, birefringence, thermo-optic coefficient (TOC), etc. Hence, thermal change plays a crucial role in an optical device's performance.

There are outnumbered research studies about NOA 68 [11, 12, 13] and other optical adhesives from Norland where the parameters mentioned above were examined. Nevertheless, there are not enough research studies about the temperature dependency of the optical transmission through the SWW that is inspected in this study. This is also verified by an optical simulation. Furthermore, the research studies do not propose anything for the durations of the internal- and external curing where the waveguide is attenuated highest that makes it very vital for the waveguide formation. This study also proposes to close this gap of the previous studies [9, 12, 14, 15, etc.].

Theoretical background helps the audiences to comprehend the literatures that underlie the setups and the simulation model.

There were some challenges to accomplish the aforementioned goal. First, the real temperature of the SWW has to be determined. It was not possible to measure the temperature directly where the SWW is located. A model for the thermal distribution was developed by Suar et al [16]. A new model based on Suar’s achievement is developed in section 3.1 corresponding to NOA 68. Moreover, the surrounding air got included to the new model where the approximated values for the approximated temperature of the SWW are accurately obtained. The optical simulation design for the waveguide is explained in section 3. Second, the classical setup of the SWW is provided and the setup prepared for the refractive index profilometer (RIPM) is explained that gives the chances to characterize the refracted-index profile (RIP) of the NOA in Chapter 4. Finally, the data are processed for the transmission through the SWW for each process of the formation and compared with the data obtained from the optical simulation.

Chapter 2: Theoretical Background

In this chapter, the previous research and knowledge about the polymerization of SWW by self-trapping, RIPM measurements, and multiphysics optical simulation will be discussed. This will shed light on the concepts outlined in this study; as a result, it will help the audience understand this research better.

2.1 Historical Background

The research studies about light-induced self-written waveguides (LISWs) or SWWs have been conducted for nearly 3 decades. The first experiment has been made by Brocklesby et al [17] in 1992. It was conducted using the ion implantation effect and its dynamic characteristics which were not comprehended completely. A year later, another experiment was performed by Frisken et al [18] in which a 532 nm laser beam was used for curing in an UV sensitive resin. It was the first experiment showed that waveguides could be formed at this wavelength.

Working principles of a SWW which is built on self-acting of light are similar to spatial solitons'. The laser beam would diffract in a planar waveguide which is made out of a photosensitive material as shown in Fig. 2.1. if we assume the incoming beam as a Gaussian one. The photosensitive material responds to the beam at the certain wavelengths where it undergoes a photopolymerization process and a permanent change in the refractive index (RI) which is corelated to the light intensity. Initially, the beam spreads out (see the top part of Fig. 2.1). However, a region is formed where the beam is most intense, and the RI increases due to the curing and the associated local density change of the material. This change in RI confines the beam in the artificial waveguide made by the beam itself. The bottom part of Fig. 2.1 shows that the beam is trapped in a certain channel which is called SWW where the beam diffraction is very small and the RI distribution is uniform along the propagation axis.

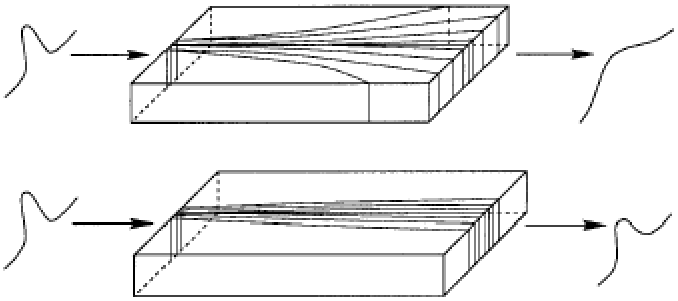

Figure 2.1 Diffraction of laser beam through a photosensitive medium. A laser beam diffracts at the beginning and then, the RI starts changing at the top and the laser beam is trapped a while later in a certain area as shown at the bottom [19].

This topic has been intensively studied during the last decades by using various photosensitive materials such as monomers, glasses, resins and others. Currently, the structure can be written by single- [20] or two-photon absorption [21, 22, 23, 24] techniques at various RI ranges, thicknesses, shapes, lengths, and wavelengths as it is needed [25, 26].

2.2 Optical Fibers and the Classifications

In this section, the general information about the optical fibers will be provided first and then, some parameters related to them will be explained detailed.

The optical fibers have a central unit (i.e., core) where the light passes through and it is surrounded by another material (i.e., cladding) whose RI is slightly lower than the core's one. This structure is also known as waveguide. Thus, total internal reflection (TIR) can occur and the light is trapped inside it. Light is guided through with the help of TIR. The process is known as waveguiding. They have to be composed of low-loss material such as silica glass. A structure similar to optical waveguide can be also formed in an adhesive that is called self-written waveguide. The optical fibers are classified mainly according to their RIs that are the step-index fiber and graded-index (GRIN) fiber or the number of modes (M) that are single-mode fiber (SMF) and multi-mode fiber (MMF) as shown in Fig. 2.2.

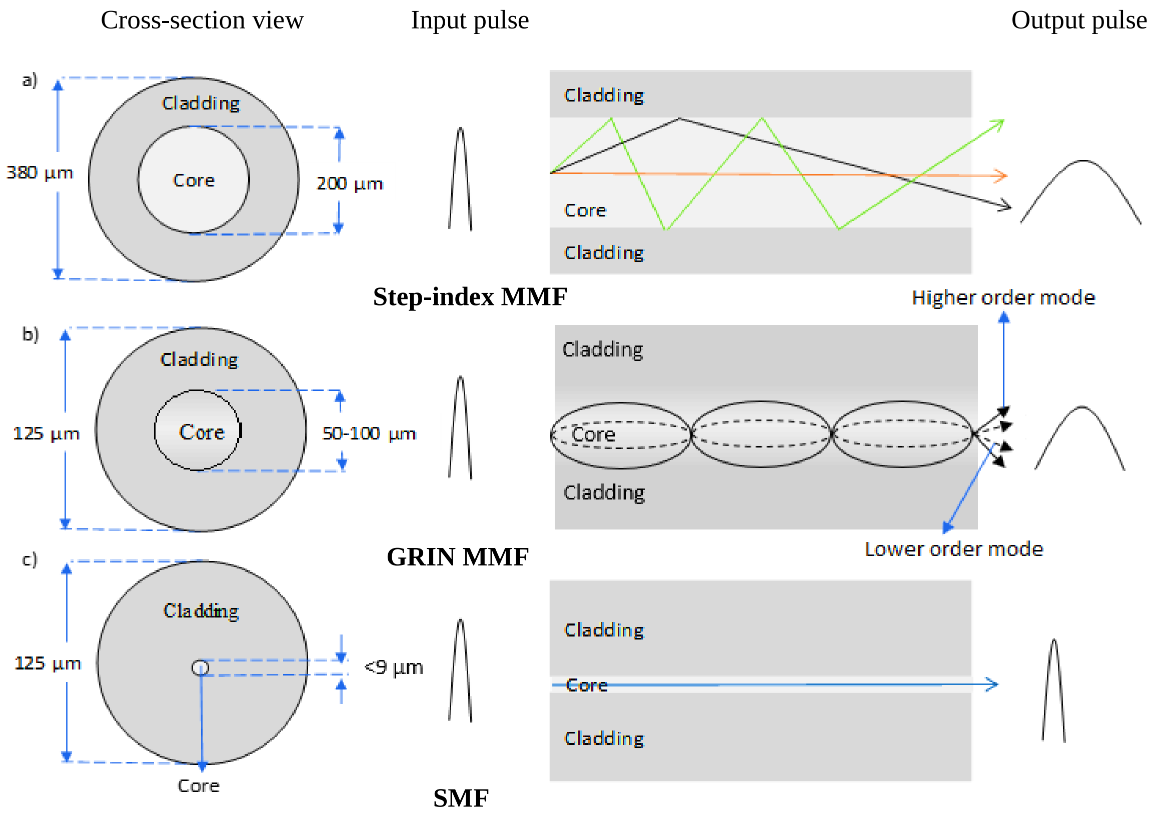

Figure 2.2 Geometry and typical rays of the optical fibers. They are classified according to the RIP and the number of transmitted modes.

RIP of GRIN fiber: GRIN MMF is a type of optical fiber where the RI is higher at the axis of the core and then it decreases gradually towards the core-cladding interface. It differs from the step-index fibers in many aspects; it has a higher bandwidth, a thinner size in diameter (~50 µm), relatively better performance, greatly reduced dispersion, travels forward in the form of sinusoidal curves (see Figure 2.2b), is used in medium-distance (10-20 km) and relatively higher speed (between 34 to 140 Mb/s) communication systems. In the GRIN MMF, the phase velocity of the beam is the lowest at the center of the fiber and increases parabolically with the radial distance, r [27]. Their RI (n(r)) is a function of it from the center (see Fig 2.3). This fact is described by the power-law function formulized for the SWW in Eq. (2.2).

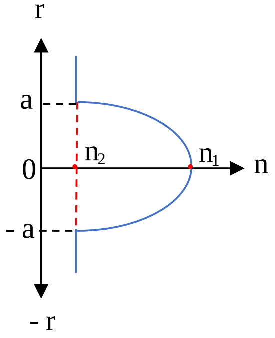

Figure 2.3 RIP of a GRIN MMF where a is the radius of the core, and n_1 and n_2 are the RIs of the core, and the cladding, respectively. The RIP of the fiber changes parabolically throughout the core and stays constant in the cladding.

$$n(r) = \begin{cases} n_1 \sqrt{1 - 2\Delta \left(\frac{r}{a}\right)^g}\ , \ \ r \leq a \\ n_1\sqrt{1-2\Delta} = n_2\ , b \geq r > a, \end{cases} \tag{2.1}$$

[28]

where b is the radius of the cladding and g is the exponent of the power function that indicates the steepness of the profile, and Δ is found by:

$$\Delta = \frac{n_1^2 - n_2^2}{2n_1^2} \tag{2.2}$$

The quantity $n^2(r)$ ultimately approaches a step function where g→∞. Thus, the step-index fiber is a special form of the GRIN fiber. The fact is depicted in Fig. 2.4. [29]

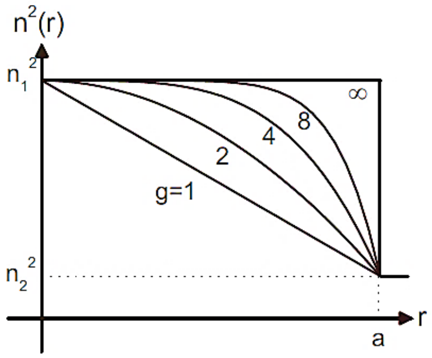

Figure 2.4 RIPs for different g values. g= 1, g=2, and g= ∞ are the profiles of a triangular profile fiber, a parabolic profile fiber, and a step-index profile fiber, respectively. The fiber becomes a step-index fiber when g goes to infinite.

Numerical aperture (NA) of the fiber: The NA of a fiber is a value for its capability of collecting light and can be calculated as:

$$NA = \sqrt{n_1^2 \, 2\Delta} \tag{2.3}$$

V and M parameters of the fiber: Commonly**,** V is used as normalized frequency parameter of a fiber. The V number is a very useful parameter to express many other parameters in terms of it, for instance, M at a specific wavelength, mode cut-off conditions, and the propagation constant. Also, it can be calculated for the GRIN fibers as follow:

$$\mathrm{V} = \frac{\pi \mathrm{d}}{\lambda} n_1 \sqrt{2\Delta} \tag{2.4}$$

where d is the diameter of the SWW and λ is the wavelength of the light. M is found by inserting V into the eq. below.

$$M = \frac{V^2}{4} \tag{2.5}$$

M is a crucial parameter to simulate the beam profile.

Confinement factor: It defines the fraction of the energy which is confined within the core. It can be simply calculated with the ratio of the modal gain and gain within the SWW at the specific wavelength (See Eq. 2.6).

$$\Gamma = \frac{modal\ gain}{gain} \tag{2.6}$$

Practically, since the fundamental transverse mode propagates in a GRIN fiber. Also, the research studies showed that its polarization does not change significantly. Because of these reasons, TE (Transverse electric) mode should be the one, most concerned within the waveguide. Botez et al. [30, 31] made a generalized approximation by using this fact (see Eq. (2.7)).

$$\Gamma \cong \frac{D^2}{D^2 + 2} \tag{2.7}$$

where Γ is the confinement factor and D is the normalized thickness of the core of the waveguide and it is calculated as follows;

$$D = 2\pi\left(\frac{d}{\lambda}\right)\sqrt{(n_1^2 - n_2^2)} \tag{2.8}$$

2.3 SWW Formation

SWW formation is a polymerization process and can be divided into 3 steps basically. The first step is the initiation where the energy is transferred to the initiators using UV-light and thus, the molecules inside the initiators are taken apart into 2. These unpaired, separated particles are named as free radicals. Here radicals play the role as reactive center. Monomer gets only in reaction with the reactive center instead of reacting with each other and form the derivatives of it such as dimer, trimer, …, and n-mer. Secondly, these radicals make chemical bonds with the monomers which are combined to form the chains. This propagation process occurs faster than the initiation process. The last step is termination where these monomer chains combines to form single-molecule polymer or two-molecule dead polymer chains. The mechanisms occur in the last step are combination and disproportion respectively. They take place simultaneously, but to different extents depending on polymer and the condition. Combination is the result of binding two macroradicals where they combine to form the one conjoined entity of sizes. On the other hand, disproportionation is also the combination of the macroradicals, but they result into two separate polymer chains. These polymer chains (e.g. dead polymers) are in a non-reactive state which means that they ended the polymerization for themselves. According to Flory et al [32], these polymerization steps explained above are repeated themselves throughout the SWW many times. More details on this topic can be found in [33].

2.3.3 Refractive Index Modulation During the Polymerization

In this part, a theoretical model will be used to explain how a SWW grows in a photosensitive medium. The polymerization process occurs relatively slow. Therefore, for any time given, the stationary wave formula of electric field envelope [34] can do this job for the light distribution which is completed by a suitable equation of RI change. A model by Monro et al [35] is built for SWW made with the scalar wave formula. Enveloping $\mathcal{E}$ is used for the slowly changing field and if we make a paraxial approximation, then the equation can be redesigned as follow:

$$2\, i\, k_0\, n_0\, \frac{\partial \mathcal{E}}{\partial Z} + \nabla_{\perp}^2 \mathcal{E} + 2\, k_0^2\, n_0\, \Delta n\, \mathcal{E} + i\, k_0\, n_0\, \alpha\, \mathcal{E} = 0 \tag{2.9}$$

where k_0 is the wave number for vacuum and calculated by $2\pi/\lambda$, n_0 is the RI in the beginning, $\nabla_{\perp}^2$ is the Laplace operator, α is the coefficient of attenuation, and Δn is the change in RIs. This equation is a generalized parabolic equation and however, because of the medium's photosensitive nature, its third term depends on time and contributes to RI change induced by laser beam. Additionally, the last part of the equation which defines the loss can also be omitted, if the loss is very small. At the end, Eq. (2.9) can be redesigned and normalized as [19];

$$i\, \frac{\partial \mathrm{E}(\mathrm{r},\ \mathrm{z}, \tau)}{\partial z} + \mathrm{D} \nabla_{\perp}^2 \mathrm{E} + \upsilon(\mathrm{r}, \mathrm{z}, \tau) \mathrm{E} = 0 \tag{2.10}$$

where E is the normalized complex envelope of electric field and found by $\mathcal{E}/\mathcal{E}_0$, z is the distance of propagation and calculated by Z/a, $r = R/a$ is the spatial coordinate in the transverse plane, τ is the ratio of final and initial times, t and t_0, D is the coefficient for the diffraction and calculated by $(2\, a\, k_0\, n_0)^{-1}$ where a is the width of the beam, and υ is $\Delta n\, a\, k_0$.

P is the normalized power and can be driven from Eq. (2.9) [19].

$$P = \int |E^2|\, dx \tag{2.11}$$

Lam et al [36] and Hand et al [37] used the correlation between the RI change and the squared of power and proposed a local model for two-photon absorption,

$$\frac{\partial \Delta n}{\partial t} = AI^2 \tag{2.12}$$

where A is a coefficient and an intrinsic property, and I is the spatial intensity of light and calculated by $I(z,t) = |E^2|$. The RI increases in the illuminated regions where $A > 0$ [38]. If the analogy with Eq. (2.12) is used for the one-photon model, then the equation will be as follow:

$$\frac{\partial \Delta n}{\partial t} \propto I \tag{2.13}$$

2.3.4 Heat Effect on the SWW

Heating the SWWs changes in two ways. Firstly, it affects the polymerization and thus, RI of the adhesive is employed in SWW formation. Secondly, it changes the polymerized core and cladding of the SWW's dynamics and also its RI. Both effects will be explained in the following section.

Heat effect during polymerization: Most of the monomers starts the polymerization process when they are heated even in the absence of initiators. The initiators are decomposed significantly at the higher temperature as well as the light-induced photochemical composites. Heating is the one of the main factors which affects the polymerization process most. An increasing temperature also increases the polymerization rate and decreases the molecular weight of the polymer.

Numerous research studies have been conducted about that topic and the results indicate that the radicals are thermally yielded from the monomer. These radicals are the products of the thermo-homolysis of the identically paired molecules. The radicals are normally involved in the polymerization process.

Initiation processes for methyl methacrylate starts with the homolysis of hydrogen molecules and then the unpaired hydrogens, free radicals, respectively, react with two monomer molecules and form monoradicals [39, 40] as shown in Eq. (2.14).

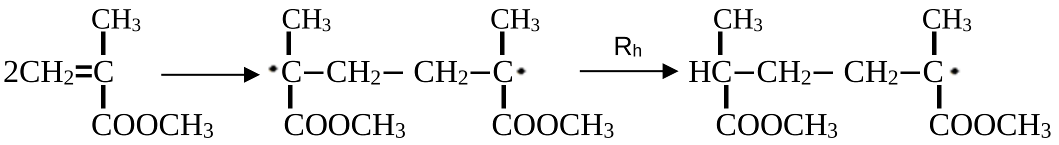

$$2CH_2{=}C(CH_3)(COOCH_3) \longrightarrow {}^{\bullet}C(CH_3)(COOCH_3){-}CH_2{-}CH_2{-}C(CH_3)(COOCH_3)^{\bullet} \xrightarrow{R_h} HC(CH_3)(COOCH_3){-}CH_2{-}CH_2{-}C(CH_3)(COOCH_3)^{\bullet} \quad (2.14)$$

In the next steps (e.g. propagation and termination) which are the same as explained in section 2.2.2, the monoradicals end up with the polymer chains.

Heat effect on polymers: Heat affects also SWW structure after the polymerization process due to it is a type of polymer. Diemeer et al. [41] made an extensive research on this fact and their study indicated that RI change is correlated with the T due to the change of density, ρ. So, TOC can be formulized as follows;

$$\frac{\mathrm{dn}}{\mathrm{dt}} = \left(\frac{\partial \mathrm{n}}{\partial \rho}\right)_{\mathrm{T}} \left(\frac{\partial \rho}{\partial \mathrm{T}}\right) + \left(\frac{\partial \mathrm{n}}{\partial \mathrm{T}}\right)_{\rho} = -\left(\frac{\rho\,\partial \mathrm{n}}{\partial \rho}\right)_{\mathrm{T}} \alpha_{\mathrm{T}} + \left(\frac{\partial \mathrm{n}}{\partial \mathrm{T}}\right)_{\rho} \qquad (2.15)$$

where n is the RI, $\mathrm{dn/dt}$ is the temperature-induced RI change, $(\rho\partial n/\partial\rho)_T$ is a constant which is specialized for each polymer material that can be found by Lorentz-Lorenz equation as shown below in Eq. (2.16), t is the time, α_{T} is the coefficient of thermal expansion (CTE), and $(\partial n/\partial \mathrm{T})_\rho$ is the RI change for a certain density.

$$\left(\frac{\rho\partial n}{\partial\rho}\right)_T = (1-\Lambda_0)\frac{(n^2+2)(n^2-1)}{6n} \qquad (2.16)$$

where Λ_0 is the strain polarizability constant discovered by Mueller et al [42] in 1935 and correlated to the change in density on atomic polarizability of the material. This value is too small for polymers because there are not significant interactions between the polymer molecules. Therefore, it has been determined as 0.15 for poly (methyl methacrylate) (PMMA) [43].

The equations can be used to estimate TOC of a polymer using CTE if n, Λ_0, and $(\partial n/\partial \mathrm{T})_\rho$are known. The measurements of all these parameters mentioned above are harder than measuring TOC from the material directly. Instead of that, the correlation between TOC and CTE is established [44], Eq. (2.15) is employed, and make an estimation for TOC. Thermally induced RI change under constant density, $(\rho\partial n/\partial\rho)_T$ for PMMA is about 4x10^{-6}/^{o}C [43].

2.4 RI index Measurement by RIPM

To realize the simulation concerning the optical response of an SWW to a change of the temperature, the values of the RI change with the temperature were needed. These values were measured using a RIPM which is based on the refracted near-field method (RNF). A brief knowledge about the method will be provided in section 2.4.1.

2.4.1 Refracted Near-Field Method

This method, introduced by Stewart et al [45] is based on the light which leaves the core from the sides through the cladding. This defines the fiber's RIP. This method completes the near-field method where the power of the trapped beam is used.

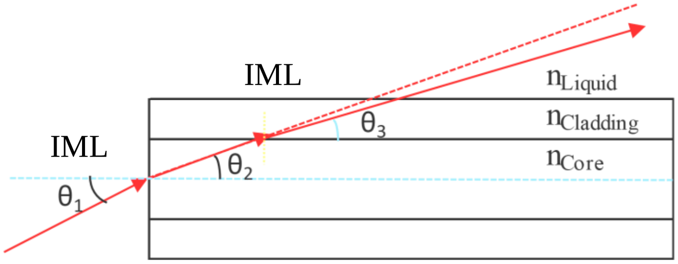

Figure 2.5 Ray trajectory for the laser beam in RNF method that follows the path from the index matching liquid (IML) through the core and the cladding of a waveguide.

The ray trajectory for this method is considered as in Fig. 2.5. The method can be explained with this sketch. Firstly, the laser beam coming from the IML whose RI is equal to the cladding enters the fiber input and exits from the boundary between core and cladding. The relationship between the RIs and the angles in the media can be formulized by Snell's law:

$$n_{core}\cos\theta_2 = n_{cladding}\, cos\,\theta_3\ [46] \tag{2.17}$$

where n_{core} is the RI of the core and $n_{cladding}$ is the cladding's RI. Here, angles between core and cladding which are parallel to their interface are used instead the ones from normal of it.

And Snell's law is applied again for first and second media:

$$n_{liquid} \sin\theta_1 = n_{core} \sin\theta_2 \tag{2.18}$$

where n_{liquid} is the RI of IML. We can derive the relationship between the input angle, θ_1 and output angle; θ_3 if Equations (2.17) and (2.18) are combined.

$$n_{liquid} \sin \theta_1 = \sqrt{n_{core}^2 - n_{liquid}^2 + n_{liquid}^2\, sin^2\theta_{3min}} \tag{2.19}$$

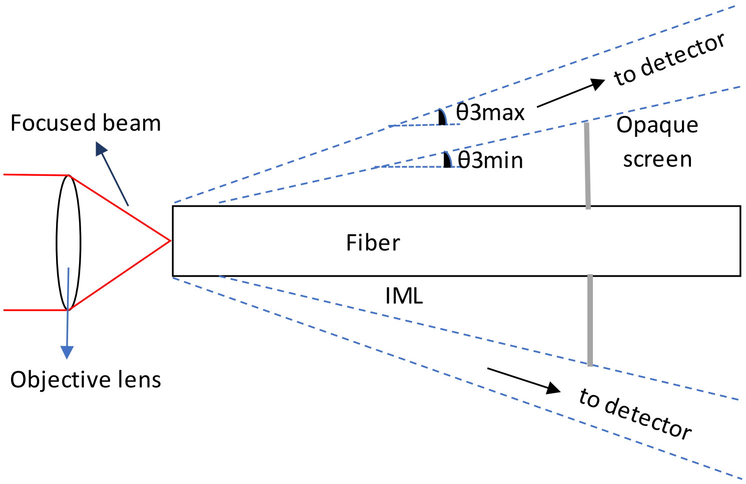

Figure 2.6 Experimental setup for RNF method. It shows the ray path from IML to the detector through the fiber and possible leaky modes.

The device that we used is based on this method and schematically shown in Fig. 2.6. In this implementation, the beam is focused to the surface of the sample fiber. Thus, most of the light can be contained inside the fiber. Some of the light exists after it enters the core and the rest will escape from the sides of core due to the leakage due to the leaky modes. Due to the amount of leaky mode power which goes to the detector, the rest which stays inside the fiber cannot be detected. Therefore, an opaque screen is placed at the minimum angle in order to block the leaky modes before they reached to the detector. The angle for the input beam which corresponds to this angle can be found by the Eq. (2.19). Nevertheless, all the light which leaves the core and hits the detector where θ_1 is greater than θ_{1min} should be observed carefully. In order to form this situation, the fiber should be immersed in to IML. This will block the reflection from cladding through the liquid.

In this step, the correlation between power at the detector and the distribution of the RI can be derived easily. The formula can be written as follows:

$$P = S\int_0^{2\pi} d\phi \int_{\theta 1\min}^{\theta 1\max} \sin\theta \, d\theta \tag{2.20}$$

If the formula is solved. The formula will be:

$$P = 2\pi S(\cos\theta_{1min} - \cos\theta_{1max}) \tag{2.21}$$

where P is the power reached to the detector and S is the light intensity at the input.

The formula above is expressed with the angle, θ_{3min} by the help of Eq. (2.19). This angle is determined by opaque screen that reduces the light hitting the detector.

$$P = 2\pi S\left[\sqrt{\cos^2\theta_{3min} - \frac{n_{core}^2 - n_{liquid}^2}{n_{core}^2}} - \cos\theta_{1max}\right] \tag{2.22}$$

Since $n_{core} - n_{liquid}$ is small. Thus, the formula can be approximated as [47]:

$$P = 2\pi S\left[cos\,\theta_{3min} - cos\,\theta_{1max} - \frac{n_{core} - n_{liquid}}{n_{liquid}\,cos\,\theta_{3min}}\right] \tag{2.23}$$

This method works most efficient and gives maximum power at the detector if the beam can be directed to the cladding. The minimum angle in the cladding, θ_{3min}, that can be found by placing the circular screen to the front of the detector. The maximum value of cone shaped light incident at the input, θ_{1max} and it can be arranged by focusing or other apertures. The cladding's RI are the parameters should be measured to find the fiber core's

RI. It is noted that P of light measured must be as a function of distance of the input beam, r that is measured from the laser source to the sample fiber.

2.5 Numerical Modeling of the Optical Simulation

In this section, I would like to introduce the theoretical foundation of the algorithms that are utilized to simulate the SWW that was created experimentally. Maxwell equations are the fundamental basis, they describe the characteristic and the interaction of EM (Electro-magnetic) waves with the materials. First, I will introduce the equations and subsequently, the beam propagation method (BPM) will be explained.

2.5.1 Maxwell's Equations

Throughout the simulations are all made in the spectral domain where monochromatic light is linked with the angular velocity ω. The spectral formulation, the subsequent notations, and discussions of Maxwell's Equations are based on the standard textbooks [48, 49, 27]. The modes of propagation for circular waveguides are generally a mixture of TE and transverse magnetic (TM) waves which are classified as hybrid modes (EH and HE modes) [50]. Since the solutions of their wave equations are very complicated, cylindrical coordinates are required to solve them. The TE and TM field components of the monochromatic light obey the Helmholtz equation shown in Eq. (2.24).

$$\frac{\partial^2 U}{\partial r^2} + \frac{1}{r}\frac{\partial U}{\partial r} + \frac{1}{r^2}\frac{\partial^2 U}{\partial \varphi^2} + \frac{\partial^2 U}{\partial z^2} + n^2\, k^2\, U = 0 \tag{2.24}$$

where $U = U(r, \varphi, z)$ represents the scalar wave function of one of the guided modes which propagates in the z-direction with the propagation constant, β. That is why the z dependence of the wave function is found in the form of $e^{-i\,\beta\,z}$. Furthermore, these are the periodic wave functions within the angle, φ with a period, 2π which can be illustrated as a harmonic function of $e^{-i\,l\,\varphi}$, where l is an integer. Thus, the scalar wave function of any mode is written as follow:

$$\mathrm{U(r,\varphi,z) = u(r)\, e^{-i\,\beta\, z}\, e^{-i\, \mathit{l}\, \varphi}}, \quad l = 0, \pm 1, \pm 2, \ldots \tag{2.25}$$

The velocity differences between the modes, material dispersion effects, and the waveguide dispersion limit the information bandwidth of the GRIN fibers [27]. It is difficult to carry out an accurate analysis of the neutral modes of a radially inhomogeneous medium. The issue is originated from the fourth-order differential equation while there would be a lot of methods for the analysis of the wave theory and the propagation characteristics of any non-uniform core profiles of fibers. Wantzel-Kramers-Brillouin (WKB) approximation, Rayleigh-Ritz, Power-series expansion, finite element, and staircase-approximation methods are developed to solve the issue [27].

The formulation of the problem is considered in cylindrical coordinates $(r, \varphi. z)$ and electric and magnetic fields are expressed by using the axial and transverse components as,

$$\vec{\mathrm{E}} = \left(\vec{\mathrm{E}}_{\mathrm{t}}\,(\mathrm{r},\varphi) + \vec{\mathrm{k}}\,\mathrm{E_z}\,(\mathrm{r},\varphi)\right) \mathrm{e}^{\mathrm{i}(\omega\, \mathrm{t}\, -\, \beta\, \mathrm{z})} \tag{2.26}$$

$$\vec{\mathrm{H}} = \left(\vec{\mathrm{H}}_{\mathrm{t}}\,(\mathrm{r},\varphi) + \vec{\mathrm{k}}\,\mathrm{H_z}(\mathrm{r},\varphi)\right)\, \mathrm{e}^{\mathrm{i}(\omega\, \mathrm{t}\, -\, \beta\, \mathrm{z})} \tag{2.27}$$

where $\vec{\mathrm{E}}_{\mathrm{t}}$ and $\vec{\mathrm{H}}_{\mathrm{t}}$ are the tangential components of electric and magnetic fields, respectively and $\mathrm{E_z}$ and $\mathrm{H_z}$ are the axial scalar components which $\vec{\mathrm{k}}$ (unit vector) shows its direction. The equations above can be substituted into the following Maxwell's equations.

$$\nabla \times \vec{\mathrm{E}} = -\mu_{\mathrm{o}}\, \frac{\partial \vec{\mathrm{H}}}{\partial \mathrm{t}} \tag{2.28}$$

$$\nabla \times \vec{\mathrm{H}} = \epsilon_{\mathrm{o}}\, \hat{\mathrm{k}}\, \frac{\partial \vec{\mathrm{E}}}{\partial \mathrm{t}} \tag{2.29}$$

$$\nabla \epsilon\, \vec{\mathrm{E}} = \rho \tag{2.30}$$

$$\nabla\, \mu\, \vec{\mathrm{H}} = 0 \tag{2.31}$$

Where ρ is the charge density, ϵ_{o} is the permittivity, μ_{o} is the and permeability of the free space, and $\vec{\mathrm{E}}$ and $\vec{\mathrm{H}}$ are electric and magnetic fields of any mode, respectively.

Then, the four differential equations in the terms of $\vec{\mathrm{E}}_\mathrm{t}$, $\vec{\mathrm{H}}_\mathrm{t}$, E_z, and H_z are obtained by making some algebraic computations [51].

$$-\mu\,\nabla\left(\frac{1}{\mu}\,\nabla\times\vec{\mathrm{E}}_\mathrm{t}\right)+(\omega^2\,\epsilon\,\mu-\beta^2)\,\vec{\mathrm{E}}_\mathrm{t}+\nabla\,\left(\frac{1}{\epsilon}\,\nabla\times\left(\epsilon\,\vec{\mathrm{E}}_\mathrm{t}\right)\right)=0 \qquad (2.32)$$

$$-\epsilon\,\nabla\left(\frac{1}{\epsilon}\,\nabla\times\vec{\mathrm{H}}_\mathrm{t}\right)+(\omega^2\,\epsilon\,\mu-\beta^2)\,\vec{\mathrm{H}}_\mathrm{t}+\nabla\,\left(\frac{1}{\mu}\,\nabla\times\left(\mu\,\vec{\mathrm{H}}_\mathrm{t}\right)\right)=0 \qquad (2.33)$$

$$\begin{aligned}&\frac{\omega^2\,\epsilon\,\mu-\beta^2}{\epsilon}\,\nabla\left(\frac{\epsilon\,\nabla\times\mathrm{E}_\mathrm{z}}{\omega^2\,\epsilon\,\mu-\beta^2}\right)+(\omega^2\,\epsilon\,\mu-\beta^2)\,\mathrm{E}_\mathrm{z}\\&\quad-\nabla\left(\log_{10}\left(\frac{\epsilon\cdot\mu}{\omega^2\cdot\epsilon\cdot\mu-\beta^2}\right)\right)\left(\vec{\mathrm{k}}\,\frac{\omega\,\mu}{\beta}\,\nabla\times\mathrm{H}_\mathrm{z}\right)=0\end{aligned} \qquad (2.34)$$

$$\begin{aligned}&\frac{\omega^2\,\varepsilon\,\mu-\beta^2}{\varepsilon}\,\nabla\left(\frac{\mu\,\nabla\times\mathrm{H}_\mathrm{z}}{\omega^2\,\varepsilon\,\mu-\beta^2}\right)+(\omega^2\,\varepsilon\,\mu-\beta^2)\,\mathrm{H}_\mathrm{z}\\&\quad-\nabla\,\left(\log_{10}\left(\frac{\varepsilon\,\mu}{\omega^2\,\varepsilon\,\mu-\beta^2}\right)\right)\,\left(\vec{\mathrm{k}}\,\frac{\omega\,\mu}{\beta}\,\nabla\times\mathrm{E}_\mathrm{z}\right)=0\end{aligned} \qquad (2.35)$$

The transverse and axial components of electric and magnetic fields are obtained by using the above equations [51].

$$\vec{\mathrm{E}}_\mathrm{t}=-\mathrm{i}\,\frac{\beta}{\omega^2\,\varepsilon\,\mu\,-\,\beta^2}\,\left(\nabla\times\mathrm{E}_\mathrm{z}-\frac{\omega\,\mu}{\beta}\,\vec{\mathrm{k}}\times\nabla\,\mathrm{H}_\mathrm{z}\right) \qquad (2.36)$$

$$\vec{\mathrm{H}}_\mathrm{t}=-\mathrm{i}\,\frac{\beta}{\omega^2\,\varepsilon\,\mu-\beta^2}\,\left(\nabla\times\mathrm{H}_\mathrm{z}-\frac{\omega\,\varepsilon}{\beta}\,\vec{\mathrm{k}}\,\nabla\times\mathrm{E}_\mathrm{z}\right) \qquad (2.37)$$

2.5.2 Vectoral and Scalar Wave Equations

The RI changes parabolically in the core and stays constant in the cladding for a GRIN MMF and it is written as;

$$n = \sqrt{\frac{\epsilon\,\mu}{\epsilon_o\,\mu_o}} \tag{2.38}$$

Although, the equality, $\mu_o = \mu$ in the fiber materials and the spatial change of RIs (n) come from ϵ. Therefore, the dielectric constant (ϵ) can be written as a function of the position (i.e., ϵ (x, y, z)). The equations would be as follows if some vector identities are used.

$$\nabla^2\vec{\mathrm{E}}_\mathrm{t} + (\omega^2\,\epsilon\,\mu - \beta^2)\,\vec{\mathrm{E}}_\mathrm{t} + \nabla\left(\frac{\nabla\epsilon}{\epsilon}\vec{\mathrm{E}}_\mathrm{t}\right) = 0 \tag{2.39}$$

$$\nabla^2\vec{H}_t + (\omega^2\,\epsilon\,\mu - \beta^2)\,\vec{H}_t + \frac{\nabla\varepsilon}{\varepsilon}\left(\nabla \times \vec{H}_t\right) = 0 \tag{2.40}$$

The equations above are known as vectoral wave equations and they are divided into 2 scalar components. Moreover, every equation has 2 simultaneous transverse parts (i.e., E_x, E_y, H_x, H_y or E_r, E_φ, H_r, H_φ) due to the existence of the third terms. However, the term is missing for the uniform-core fibers. Therefore, two transverse field components can be separated. The scalar wave equation is obtained if only the approximation is implemented. [51]. The equations are transformed into the ones below if the term is neglected and the ratio of $\nabla\varepsilon/\varepsilon$ is taken as very small. This approximation is named as 'small index gradient' or 'weakly guiding approximation'.

$$\nabla^2\vec{\mathrm{E}}_\mathrm{t} + (\omega^2\,\epsilon\,\mu - \beta^2)\,\vec{\mathrm{E}}_\mathrm{t} = 0, \tag{2.41}$$

$$\nabla^2\vec{\mathrm{H}}_\mathrm{t} + (\omega^2\,\epsilon\,\mu - \beta^2)\,\vec{\mathrm{H}}_\mathrm{t} = 0 \tag{2.42}$$

Ultimately, scalar wave equations are obtained by dividing these equations into x and y components.

$$\nabla^2\mathrm{E}_\mathrm{a} + (\omega^2\,\epsilon\,\mu - \beta^2)\,\mathrm{E}_\mathrm{a} = 0, \qquad \left(\mathrm{E}_\mathrm{a} = \mathrm{E}_\mathrm{x},\ \mathrm{E}_\mathrm{y}\right) \tag{2.43}$$

$$\nabla^2\mathrm{H}_\mathrm{a} + (\omega^2\,\epsilon\,\mu - \beta^2)\,\mathrm{H}_\mathrm{a} = 0 \qquad \left(\mathrm{H}_\mathrm{a} = \mathrm{H}_\mathrm{x},\ \mathrm{H}_\mathrm{y}\right) \tag{2.44}$$

Now, these equations are needed to be written in the cylindrical coordinate system where electric field is only considered.

$$\nabla^2 \mathrm{E_r} - \frac{1}{r^2}\,\mathrm{E_r} - \frac{2}{r^2}\,\frac{\partial E_\varphi}{\partial \varphi} + (\omega^2\,\epsilon(r)\,\mu_0 - \beta^2)\,\mathrm{E_r} = 0 \tag{2.45}$$

$$\nabla^2 \mathrm{E}_\varphi - \frac{1}{r^2}\,\mathrm{E}_\varphi - \frac{2}{r^2}\,\frac{\partial E_\varphi}{\partial \varphi} + (\omega^2\,\epsilon(r)\,\mu_0 - \beta^2)\,\mathrm{E}_\varphi = 0 \tag{2.46}$$

The equations will turn into as follows if the coordinate system is changed and they are rewritten as indivisible [51].

$$\mathrm{E_r^{(j)}} = \pm\,\mathrm{i}\,\mathrm{R^{(j)}(r)}\,\mathrm{e}^{-\mathrm{i\,m}\,\varphi} \tag{2.47}$$

$$\mathrm{E}_\varphi^{(\mathrm{j})} = \mathrm{R^{(j)}(r)}\,\mathrm{e}^{-\mathrm{i\,m}\,\varphi} \tag{2.48}$$

where R(r) relates to the cross-section of the cylinder as function of its radius r, Z (z) to the axes z of the cylinder, V (φ) to the azimuth angle φ, and T(t) stands for the time dependence where j takes the values of 1or 2. Lastly, two linearly independent solutions are obtained where the upper and lower signs provide j=1 and j=2, respectively, if the new variable is substituted into the equations (see Eq. (2.45) and (2.46)).

$$\frac{1}{\mathrm{r}}\,\frac{\mathrm{d}}{\mathrm{dr}}\left(\mathrm{r}\,\frac{\mathrm{dR^{(j)}}}{\mathrm{dr}}\right) + \left(\omega^2\,\epsilon(\mathrm{r})\,\mu_\mathrm{o} - \beta^2 - \frac{(\mathrm{m} \mp 1)^2}{\mathrm{r}^2}\right)\mathrm{R^{(i)}} = 0 \tag{2.49}$$

The scalar wave equation could be written as follows if the components of the electric field (i.e., E_x and E_y) are rewritten with the new variable, R.

$$\frac{1}{r}\,\frac{d}{dr}\left(r\,\frac{dR}{dr}\right) + \left(\omega^2\,\epsilon(r)\,\mu_o - \beta^2 - \frac{m^2}{r^2}\right) R = 0 \tag{2.50}$$

Gradient-index terms and the solutions of the modes can be included into the equations. Thus, the equations can be rewritten for the graded-index fiber. The approximations are revealed and the arbitrary permittivity distribution is assumed [52] as:

$$\epsilon(\mathrm{r}) = \begin{cases} \epsilon_1\left(1-\mathrm{h(r)}\right), & \mathrm{r} \leq \mathrm{a} \text{ and } \mathrm{h(r)} \geq 0 \\ \epsilon_2, & \mathrm{r} > \mathrm{a} \end{cases} \tag{2.51}$$

where, a is the radius of the fiber core and ε_1 and ε_2 are the permittivity of cladding and the core where the RI of the core peaks in it, respectively. The RIs are written by:

$$\mathrm{n}_1 = \sqrt{\frac{\epsilon_1}{\epsilon_2}} \text{ and } \mathrm{n}_2 = \sqrt{\frac{\epsilon_2}{\epsilon_0}} \tag{2.52}$$

where ϵ_0 is the dielectric permittivity in vacuum.

Initially, the axial components are solved from the differential equations (2.34) and (2.35). The transverse field components (i.e., E_z and H_z) are acquired by using the equations (2.53) and (2.54).

$$E_z = \frac{\omega^2\, \epsilon_1\, \mu_o}{\beta}\, \Phi(r)\, e^{i\,(n\,\varphi+\theta)} \tag{2.53}$$

$$H_z = \omega\, \epsilon_1\, \Psi(r)\, e^{i\left(n\,\varphi+\theta-\frac{\pi}{2}\right)} \tag{2.54}$$

where n is the integer and θ is either 0 or $\pi/2$. Furthermore, $\Phi(r)$ and $\Psi(r)$ are functions of r. The following equations are obtained if they are substituted into the equations (2.34) and (2.35):

$$\frac{\chi-\mathrm{h}}{1-\mathrm{h}}\,\frac{1}{\mathrm{r}}\,\frac{\mathrm{d}}{\mathrm{dr}}\left(\left(\frac{1-\mathrm{h}}{\chi-\mathrm{h}}\right)\mathrm{r}\,\frac{\mathrm{d}\Phi}{\mathrm{dr}}\right) + \left(\omega^2\,\epsilon_1\,\mu_\mathrm{o}\,(\chi-\mathrm{h}) - \frac{\mathrm{n}^2}{\mathrm{r}^2}\right)\Phi$$

$$+\frac{\mathrm{n}}{\mathrm{r}}\,\Psi\,\left(\frac{\chi-\mathrm{h}}{1-\mathrm{h}}\right)\frac{\mathrm{d}}{\mathrm{dr}}\left(\frac{1-\mathrm{h}}{\chi-\mathrm{h}}\right) = 0 \tag{2.55}$$

$$(\chi-h)\,\frac{1}{r}\,\frac{d}{dr}\left(\left(\frac{1}{\chi-h}\right)r\,\frac{d\Psi}{dr}\right) + \left(\omega^2\,\epsilon_1\,\mu_o\,(\chi-h) - \frac{n^2}{r^2}\right)$$

$$+\frac{n}{r}\,\Phi\,(\chi-h)\,\frac{d}{dr}\left(\frac{1}{\chi-h}\right) = 0 \tag{2.56}$$

On the other hand, the transverse field components in the terms of Φ and Ψ can be expressed as follows if the Equations (2.55) and (2.56) are inserted into (2.36) and (2.37):

$$E_r = -i\ \frac{1}{\chi - h} \left(\frac{d\Phi}{dr} + \frac{n}{r}\ \Psi\right)\ e^{i\,(n\,\varphi\,+\,\theta)} \tag{2.57}$$

$$E_\varphi = i\ \frac{1}{\chi - h} \left(\frac{d\Psi}{dr} + \frac{n}{r}\ \Phi\right)\ e^{i\left(n\,\varphi\,+\,\theta\,-\,\frac{\pi}{2}\right)} \tag{2.58}$$

$$H_r = -i\ \frac{\beta}{\omega\ \mu_o}\ \frac{1}{\chi - h} \left(\frac{d\Psi}{dr} + \left(\frac{1 - h}{1 - \chi}\right) \frac{n}{r}\ \Phi\right)\ e^{i\left(n\,\varphi\,+\,\theta\,-\,\frac{\pi}{2}\right)} \tag{2.59}$$

$$H_\varphi = -i\ \frac{\beta}{\omega\ \mu_o}\ \frac{1}{\chi - h} \left(\left(\frac{1 - h}{1 - \chi}\right) \frac{d\Phi}{dr}\ \frac{n}{r}\ \Psi\right) \cdot e^{i\,(n\,\varphi\,+\,\theta)} \tag{2.60}$$

Now, the equations turned into much simpler ones and they are the solutions that are grouped and corresponds to the TE, TM, EH, and HE. EH and HE are the hybrid modes where the TM and TE components dominate, respectively. n = 0 is the result of the linear combination of TE and TM. Hybrid modes correspond to all the cases where n ≠ 0.

2.5.3 Beam Propagation Methods

The algorithms of the BPMs for the simulation enable us to make the analysis of the integrated photonic devices such as waveguides, SWWs, etc. Over the years, many methods have been proposed that emerge the different types of formulations [53, 54]. Further details can be obtained from the book of Kawano et al. [55]

The BPMs were correctly established for the waveguides. They solve the electric field based on the time-harmonic equation for devices and systems where it is defined as the product of changing envelope function in a slow manner and changing phase function quickly [56]. The approximation which was developed for this purpose is called slowly varying envelope approximation (SVEA). It can be implemented where the forward-propagating wave envelope changes slowly during its travel. The time-harmonic field for the longitudinally constant structures can be stated with the product of slowly changing envelope ψ and rapid oscillatory phase term $e^{-i\,\beta\,z}$ as:

$$E(x, y, z, t) = \Psi(x, y) e^{-i(\omega t - \beta z)} \tag{2.61}$$

where $\beta = k\, n_{ref}$ is the propagation constant and n_{ref} is the reference RI. The field can be directed either x or y (i.e., $E(x, y, z) = \Psi(x, y) e^{-i \beta z}$). The substitution of Equation (2.61) into the equations for the semi-vectorial wave equations [57] results in the semi-vectorial wave equations for x-directed component as:

$$2\, i\, \beta \frac{\partial \Psi}{\partial z} = \frac{\partial}{\partial x}\left[\frac{1}{n_r^2} \frac{\partial}{\partial x}(n_r^2 \Psi)\right] + \frac{\partial^2 \Psi}{\partial y^2} + \frac{\partial^2 \Psi}{\partial z^2} + (k^2\, n_r^2 - \beta^2)\Psi \qquad 2.62$$

The second order derivation in the equation is very small, so it can be neglected if the envelope Ψ changes slowly with respect to the propagation axes, z.

$$2\, i\, \beta \left|\frac{\partial \Psi}{\partial z}\right| \gg \left|\frac{\partial^2 \Psi}{\partial z^2}\right| \qquad 2.63$$

After the calculation above, the Eq. (2.62) transforms into the paraxial approximation as follows:

$$2\, i\, \beta \frac{\partial \Psi}{\partial z} = \frac{\partial}{\partial x}\left[\frac{1}{n_r^2} \frac{\partial}{\partial x}(n_r^2 \Psi)\right] + \frac{\partial^2 \Psi}{\partial y^2} + (k^2\, n_r^2 - \beta^2)\Psi \qquad 2.64$$

This equation becomes simpler for the weakly guiding structure with the low index contrast by neglecting the term, $\frac{\partial}{\partial x}\left[\frac{1}{n_r^2} \frac{\partial}{\partial x}(n_r^2 \Psi)\right]$. In this case, the propagating field can be assumed as a scalar wave and a more simplified version of the equation is:

$$2\, i\, \beta \frac{\partial \Psi}{\partial z} = \frac{\partial^2 \Psi}{\partial x^2} + \frac{\partial^2 \Psi}{\partial y^2} + (k^2\, n_r^2 - \beta^2)\Psi \qquad 2.65$$

Chapter 3: Multiphysics Simulation

The Finite Element Method (FEM) has been developed as an indispensable key technology for the modeling and the simulation of advanced engineering systems in various fields like housing, transportation, communications, mechanical stress, etc...

In building such complex systems, engineers and designers go through a sophisticated process of modeling, simulation, visualization, analysis, designing, prototyping, testing, and fabrication. To minimize faults during the process chain, a detailed simulation at the beginning of this process is necessary. This is to ensure the workability of the completed product, as well as the cost-effectiveness. The process is illustrated as a flowchart in Fig. 3.1. This process is often iterative in nature, meaning that some of the procedures are repeated based on the results obtained at a current stage to achieve an optimal performance at the lowest cost for the system to be built. Therefore, the techniques related to modeling and simulation in a rapidly and effectively play an increasingly important role, resulting in the application of the FEM being multiplied numerous times because of this.

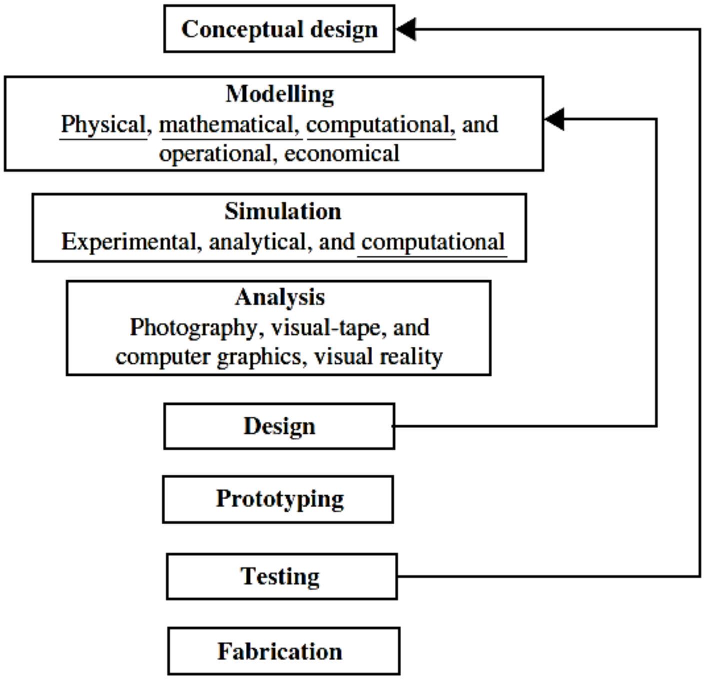

Figure 3.1 Processes leading to the fabrication of advanced engineering systems. Hereby, it is seen that simulation is the first step that helps the production [56].

Multiphysics software packages such as FEATOOL and COMSOL are used in this project that contain physics, finite element analysis (FEA) and partial differential equation (PDE) simulation toolbox. The simulations from the numerous fields in physics such as heat transfer, fluid dynamics, chemical engineering, structural mechanics, fluid-structure interaction (FSI), and electromagnetics can be fully modeled. The software packages were employed and used by the academic research studies for teaching [59, 60] and also in the industrial engineering simulation works [61, 62]. The physics modules embedded in the software can be used or a PDE equation can be customized via the softwares in 1D, 2D, or 3D. The steps implemented in the software are illustrated in Fig. 3.2.

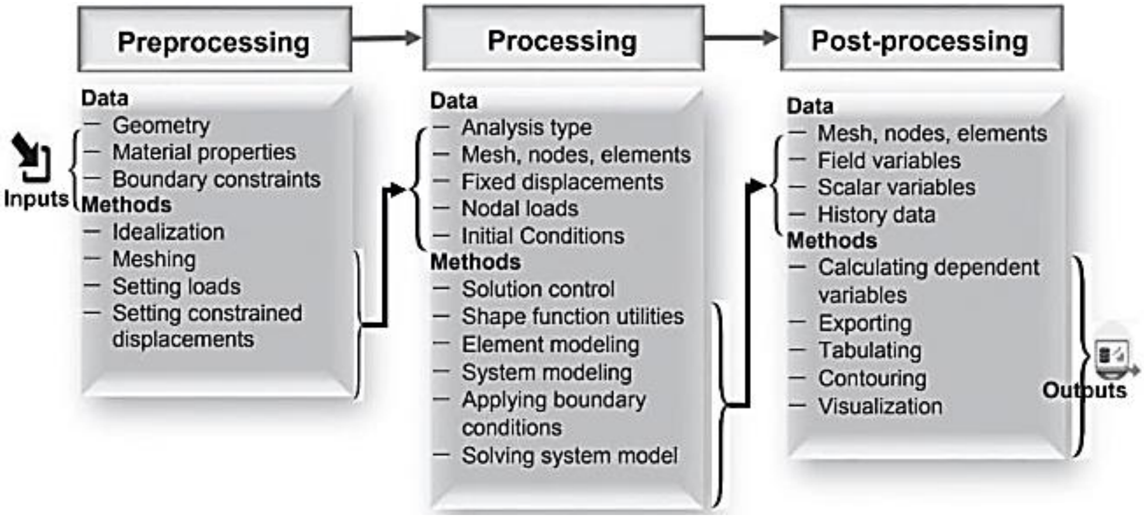

Figure 3.2 Typical data and methods in the procedure of FEA modeling. All the steps followed for the simulation are listed [58].

3.1 Thermal Simulation Design

In this chapter, the simulation steps of the thermal simulation will be explained, respectively. The steps differ for the heating and cooling processes only in the definition of the equations and the boundary conditions which are explained in section 3.1.4 and 3.1.5. The explanations of the processes are made separately for each module. FEATOOL Heat transfer module is employed and additionally, its technical details such as the dimension, the geometrical design, the mesh/grid size, the definition of the equation, the boundary conditions, solving/computing of the problem, visualization/postprocessing of the result of the numerical modeling of thermal simulation will be provided in this chapter.

A thermal simulation for the SWW was required to verify the experimental data and to understand the internal processes. Therefore, it is a crucial part of the project to get more accurate results. FEATOOL Multiphysics software is very effective when building a scientific model, provides the data for any point for the parameters such as temperature, stress, etc. from the model as it is required.

FEATOOL Multiphysics is a fully integrated physics and PDE simulation environment where the modeling process is subdivided into six steps; preprocessing (CAD and geometry modeling), mesh and grid generation, physics and PDE specification, boundary condition specification, solution, post-processing, and visualization. Now, those steps that were made before running the simulations will be explained.

3.1.1 Dimension Selection

The model is designed 2-dimensional (2D) to minimize the required computing power.

3.1.2 Geometrical Design

In this step, the shape of the model is created (see Fig. 3.3) so that it becomes so similar to the real experimental setup shown in Fig. 4.4. The SWW, the claddings, and the aluminum plate are represented by domains 4, 3 and 5, and 2 respectively and determined as 50 μm thick for each as shown in Fig. 3.3. Domain 1 is the combined subject which is obtained by subtracting/extracting domains 2, 3, 4, and 5 from the area that covers the whole area in Fig. 3.3 and represents the air, it surrounds the inner domains by a 50 μm thickness layer. The aluminum plate under the experimental setup of SWW is assumed as a heater. The coordinate system starts from the bottom left corner which is taken as (0, 0) for the x- and z-axes. The shorter side is taken as the x-axis and the longer side where also the light propagates is the z-axis.

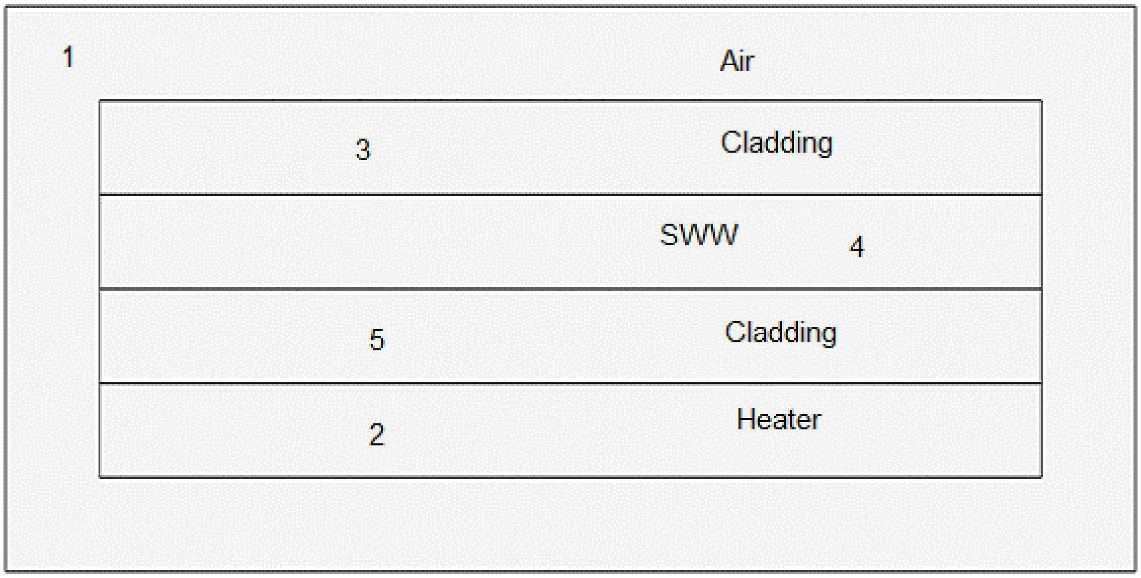

Figure 3.3 Geometry of the model for the domains. It is designed as similar as possible to the real experimental setup.

3.1.3 Mesh Generation for the Domains

The meshes are the small parts of the materials. The simulation is run for each. To get the most accurate results for the parameters needed (e.g. temperature, stress, strain, deformation), the meshes should be as small as possible. The grid size of the model is chosen as 3.1 μm as shown in Fig. 3.4. This is the minimum value provided by the software. Since the change of the temperature from one grid to another is very small, this mesh size would be sufficient to get the accurate results.

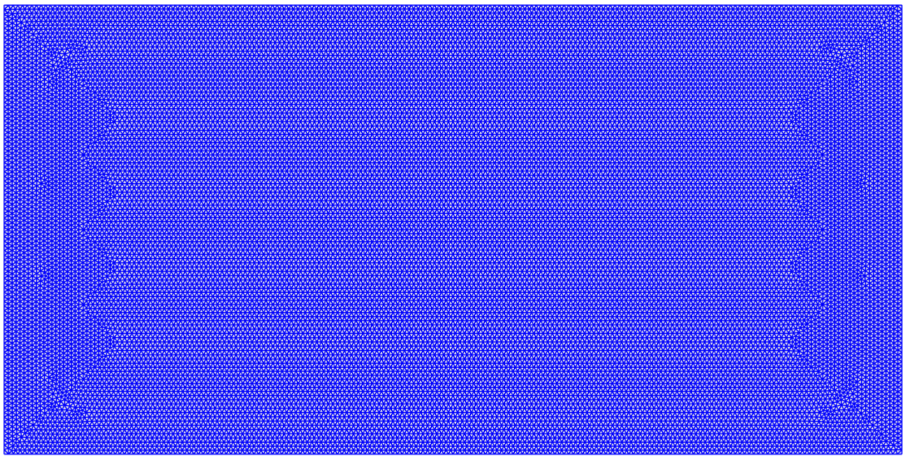

Figure 3.4 Mesh of the model for the domains. They are divided into the small parts called meshes and then, the thermal simulation is made for each mesh separately.

3.1.4 Definition of the Equation of the Domains

The equations and coefficients are defined for the domains of the model. Also, FEATool allows us to describe and enter the customized equations manually. Equations (PDEs) and model coefficients are specified in subdomain/equation mode to describe the physical phenomena to be modeled. Equations are pre-defined for many types of physical phenomena such as heat transfer, structural strains and stresses, and fluid flow. Moreover, FEATool also allows arbitrary and custom systems of PDE equations to be described and entered [63]. In the following section, the equations that were used for the simulations in this project will be explained detailed.

Heat is transferred by the conduction for our case. Therefore, we extracted the parts for convection and radiation from the equation. The mathematical equation that we used in the thermal simulation is;

$$\rho\, C_p\, T' + \nabla\,(-k\,\nabla T) = Q \tag{3.1}$$

where T is the temperature, ρ is the density, C_p is the specific heat, and k is the thermal conductivity. The parameters used in the simulation are as follows;

Table 3.1: The parameters used in the thermal simulation [16]

	ρ [kg/m^3]	Cp [J/kg °C]	k [W/m °C]
Cured NOA 68	1156	1890	0.147
SWW	1190	1500	0.25
Heater	2700	940	222
Air	1.184	1007	0.02551

C_p and k of heater do not change significantly by T as indicated in the research studies [64]. The densities depend on the CTEs of the materials as it is formulized below:

$$\rho = \frac{\rho_0}{1 + \alpha\,\Delta T} \tag{3.2}$$

Their densities were taken as constant by increasing temperature during the simulation since the CTEs of the materials are too low to affect the densities. The thermal conductivities of cured NOA 68 and SWW were extracted from the graphs [65] and their specific heats are calculated according to the formula developed by Pavlinov et al [66]. All the parameters for air were listed in [67, 68]. All the values acquired from the references and the calculations for ρ, Cp, and k are implemented to each temperature from 20 ^{o}C to 60 ^{o}C by 5 ^{o}C steps.

3.1.5 Boundary Conditions

The air that surrounds the waveguide and the heater are taken as the heating and the cooling sources. The cooling where the air is the only heat source that changes the temperature of the other domains because the power supply stops providing the energy to the heater during the cooling. Fig. 3.5 depicts the boundaries for the domains. The boundary conditions for the heating are set as $T= T_0$ for all the boundaries related to air, numbered as 1, 2, 3, and 4 and $T=T_{heater}$ is taken for all the boundaries of the heater, numbered as 5, 6, 7, and 16. The interior boundaries of the model where claddings and SWW are located, are set as continuity in the simulation. These boundaries make the domains that are not the heat sources but they are thermally in the interactions among each other and air. They are represented with the numbers; 8, 9, 10, 11, 12, 13, 14, 15, and 17 in Fig. 3.5 For the cooling, the same model (see Fig. 3.5) is used. However, the boundaries of the heater should be set as continuity because it is not a heat source anymore as explained before. Therefore, interior boundaries for the cooling will be 5, 6, 7, 8, 9, 10, 11, 12, 13, 14, 15, 16, and 17.

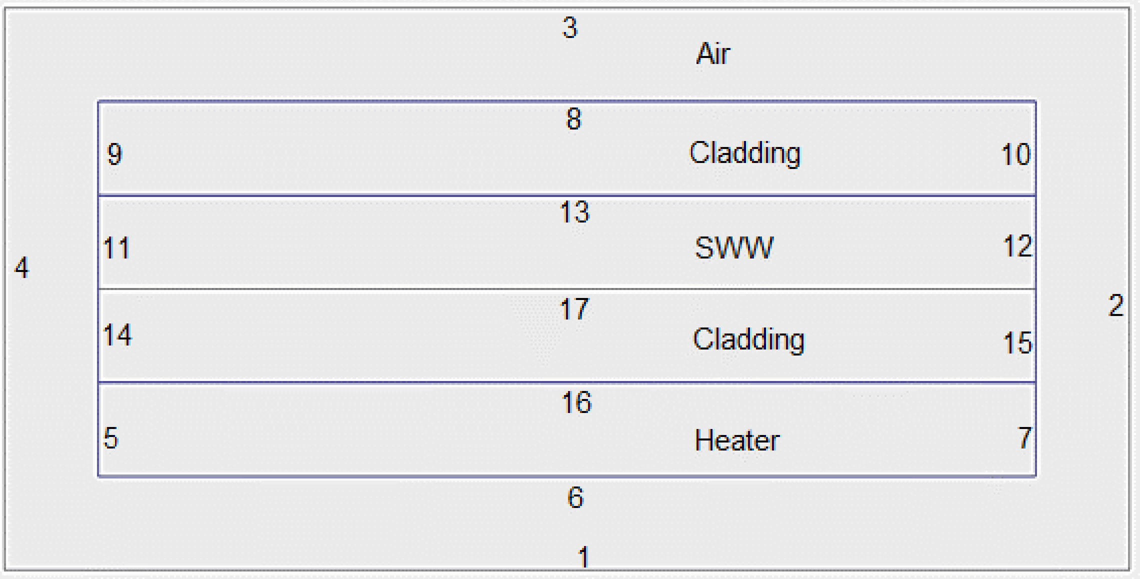

Figure 3.5 Model boundaries. They indicate if the domains behave as a heat source or any material that exchanges heat with the surroundings.

3.1.6 Solving the Problem for the Domains

In the previous steps, the problem is specified completely. Now, a suitable solver mentioned in the first part of this chapter can compute the discretized system and solve the simultaneous equations for the field variables at the nodes of the mesh. This is the most advanced computer hardware demanding process. Different software packages use various algorithms depending on the physical phenomenon to be simulated. There are two essential considerations while selecting an algorithm for solving a system of equations: the first one is the required storage, and the second one is the CPU (Central Processing Unit) time needed [69]. FEATool does this work either by default MATLAB linear solvers or use an external one such as FEniCS, SU2 CFD, or OpenFOAM solvers.

3.1.7 Visualization/Postprocessing of the Results

The digital data that is obtained by solving the equation in the previous section usually has a large volume. The results have to be visualized in such a way that it is easy to interpolate, analyze and present. The postprocessing of the results is accomplished through a so-called post-processing, usually associated with the software. Any information such as temperature, deformation, etc. at any point or a 2D cut line chosen can be obtained at this place. The object can be displayed in the form of wire-frames, a group of elements, and groups of nodes. The user can rotate, translate and zoom into and out of the objects. The field variables mentioned above can be put into graphs on the object with assisting tools such as wire-frames, fringes, contours, and deformations. The other tools are also used to obtain the iso-surfaces or, the vector fields of variable(s). Moreover, tools are available to enrich the visual effects such as lighting, shading, and shrinking [69]. Some examples can be seen in the results of this study.

3.2 Optical Simulation

In this chapter, the optical simulation will be explained. The steps are ordered chronologically. The optical simulation is made in our project in order to compare the experimental and the simulation results. The designed model is based on electromagnetic wave propagation and can be implemented to the real laboratory conditions easily. An Electromagnetic Waves, Beam Envelopes (EWBE) interface/module is employed. The optical modeling is pretty similar at some points to the ones of thermal simulation explained in Chapter 3. Those general points will not be mentioned again in this section as detailed as before. The steps followed before starting the simulation will be provided step by step.

3.2.1 Simulation Pre-settings

The dimension of the model has to be selected first. This selection depends on complexity of the model. In this project, only a basic waveguide is modeled. Therefore, a 3D model is chosen. The simulation works flawlessly for it. In the second step, the module is chosen as EWBE interface/module found under the wave optics branch provided by COMSOL multi-physics. Finally, the study type is marked as boundary mode analysis.

3.2.2 Geometrical Design

The model is designed as close as possible to the one in the experimental setup. The domains in the inner and outer circles, which were shown in Fig. 3.6, represent the SWW and the cladding respectively. Their radii are determined as 25 μm which was measured from the experiments, and 50 μm which had a real value of ~ 1 mm. For the sake of better observation, this value is chosen as 50 μm. This change affects the transmission insignificantly that is as low as 0.02 percent. The lengths of the domains are 500 μm for both as in the real setup.

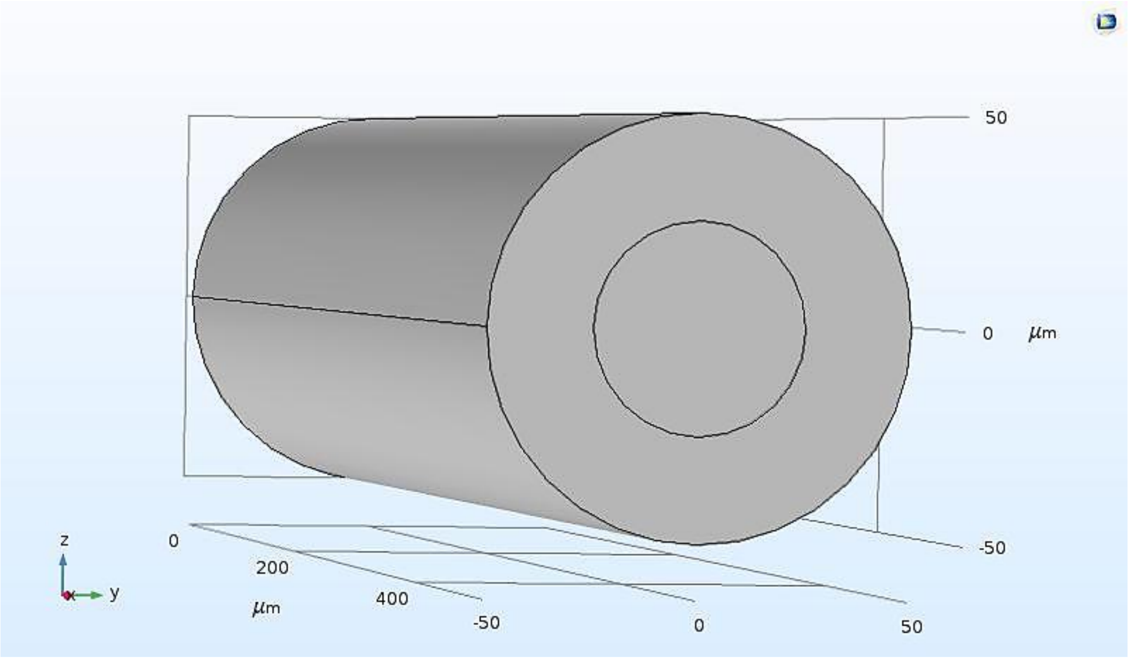

Figure 3.6 Geometry of optical simulation model. The inner and outer domains represent the core and cladding and their radii are 25 μm and 50 μm, respectively. Their height is 500 μm for both.

3.2.3 Insertion of Parameters

The operating wavelength and frequency are entered as 638 nm and 4.7×10^{14} Hz, respectively, in the software. The frequency is calculated by the formula, $f = c/\lambda$. The other necessary parameters of the simulation are the RIs of the core (e.g. SWW) and the cladding (e.g. the externally cured NOA 68) that are measured via RIPM by 5 ºC T increments in a range from 25 ºC to 60 ºC.

3.2.4 Settings for Electromagnetic Waves, Beam Envelopes Module

COMSOL software employs SVEA and make the computation for the equation explained in section 2.4.3.

The following settings are made under EWBE interface:

Wave vector, k: It is chosen as ewbe.beta_1 which suits if the number of direction is preferred as unidirectional and the equation of E would be:

$$\mathrm{E(r)} = \mathrm{E_1(r)}\, \mathrm{e}^{(-\mathrm{i}\, \mathrm{k_1}\, \mathrm{r})} \tag{3.3}$$

where E_1 represents the electric field envelope and $\mathrm{e}^{(-\mathrm{i}\, \mathrm{k_1}\, \mathrm{r})}$ is the defined quickly changing phase function.

Ports: The ports define the input and output of the laser beam. Here, port 1 is chosen as the input where the wave excitation exists with 6.5 mW power input and port 2 is set as the output where there is no excitation. To obtain the results of Reflectance (R), Absorptance (A), Transmittance (T) and effective refractive index (N_{eff}), the types of the ports are chosen as numeric which works well with boundary mode analysis. They were chosen as circular which gives the opportunity to make the simulation according to the number of modes. Additionally, circular port reference axes must be determined under the type of the port. The points of them were chosen on the periphery of the core domain shown in Fig. 3.7 with the blue rectangular dots.

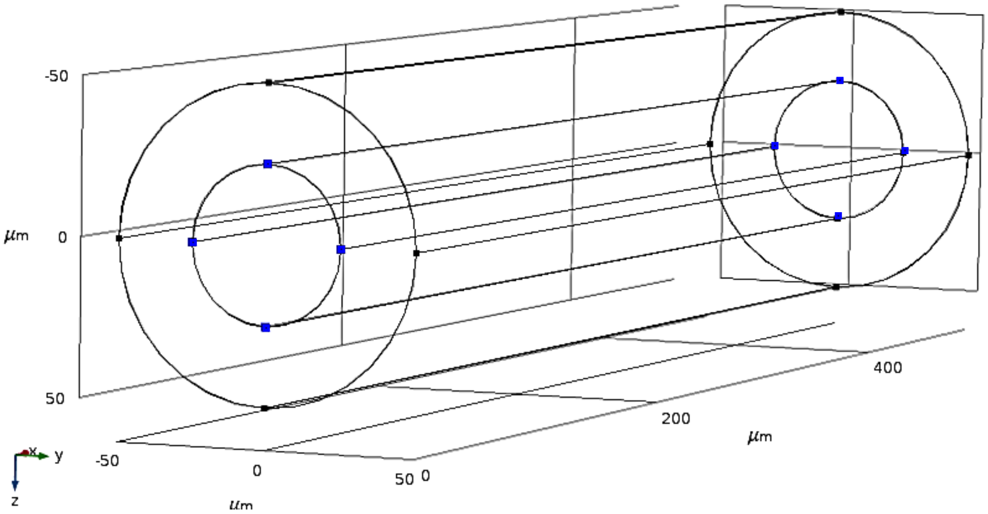

Figure 3.7 Nodes for the circular ports where port 1 and port 2 are located on the left and the right of the picture, respectively.

Boundary conditions: Scattering boundary condition is added for everything around the core to get rid of the reflections coming back from the cladding. Thus, the results become more accurate.

3.2.5 Mesh Generation of the Domains

The sequence type and the element size were chosen as physics-controlled mesh and were extremely fine shown in Fig. 3.8 which is the mesh size to obtain the best results. Physics-controlled mesh in wave vector section under EWBE module is enabled. The mesh type is selected as swept mesh containing the numbers of transverse (N_T) and longitudinal (N_L) mesh elements as 10. Thus, the results are refined.

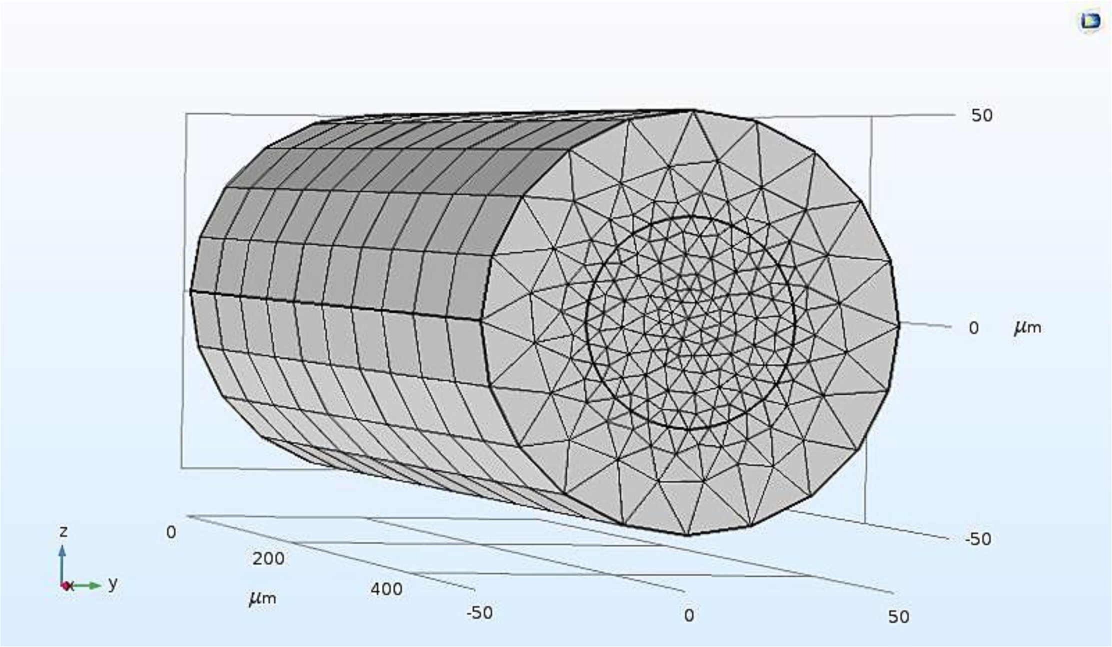

Figure 3.8 Mesh of the 3D-model of the simulated SWW. The simulation is repeated for each mesh shown in the figure.

3.2.6 Study Types and Computation

In this section, the types of study are defined and the computation is made. Boundary mode analysis is set as the study type and appointed for each port besides frequency domain. Transform, mode search method, and search for modes around under the study settings section are set as effective mode index, manual and the RI of core respectively. These settings were the same for both of the ports. This type of study provides us the results.

3.2.7 Obtaining the Results from the Simulation

In order to get the results that were mentioned in the previous part, the expressions under the global evaluation under the results section must be preset. The settings are entered as ewbe.Ttotal, ewbe.Rtotal, ewbe.Atotal, and ewbe.neff_2 for R, A, T, and Neff, respectively. The picturized electric field can be seen in the electric field (ewbe) section under the results section.

Chapter 4: Experimental Setups of SWW and RIPM

In this chapter, the technical details of the experimental setups for characterizing the SWW and measuring the RI will be provided in this chapter. They include the preferences of the materials used with the reasons why they were chosen, experimental designs, and the special techniques used to process the obtained data from the experiments. The explanations are supported by the original experimental pictures, research studies and the material specifications from their datasheets.

4.1 Experimental Setup of SWW

4.1.1 Adhesive Selection

NOA 68 is an excellent adhesive that bonds from glass to glass, glass to plastic, and plastic to plastic and has great flexibility that enables it to possess the dimensional stability for the long duration and reduce the stress during the curing. This adhesive can be employed to make a SWW up to 65 °C and will not result in an unwanted exothermic polymerization. NOA 68 has a flashpoint of 175 °C which indicates that it will not exhibit a highly flammable behavior in our experiment's operating temperature from 25 °C to 60°C. Also, the decomposition temperature that is specified at 300 °C where the polymerization process is reversed, is very high [70]. Other reasons to prefer this adhesive that it can be used unaidedly by another adhesive, doesn't need another supportive material in a one-photon approach and can be cured by UV light easily. So, it can be used for the core and the cladding both. These features make NOA 68 suitable to be used for our project.

4.1.2 Fiber Selection

Waveguides can be fabricated successfully with the help of an SMF or, an MMF in a photopolymerizable resin. An SMF has a very small core size (i.e., <9 μm, depending on the used wavelength). Therefore, it results in shorter and sharper focused lightwave and hence, SWW. Contrary, an MMF makes a spatially larger lightwave and hence, SWW.

Additionally, MMFs provide stronger and finer waveguide geometries because they have a more diffuse input lightwave [71]. Also, according to the simulations that we made with both types of fibers, MMFs have a very low loss through SWW. Due to the reasons mentioned above, MMFs have more advantages than SMFs to be preferred. OM2 class MMFs are used for this project which have a 50 μm diameter core and a 125 μm diameter cladding through which hundreds of modes can be sent through that makes this fiber suitable for this study.

4.1.3 Prebaking

NOA 68 possesses a very good adhesivity and resistance to a solvent if it is cured entirely. To obtain this optimum adhesion from the adhesive, it is placed in a vacuum oven (Thermo Scientific™ Vacutherm) where it was heated up at 50° C for 12 hours as it is shown in Fig. 4.1. This step is necessary to remove the remaining air which is ligated in the material to avoid blistering during the writing and curing steps. This is emphasized in NOA 68 material safety data sheet [70].

Figure 4.1 Vacuum oven using for aging. It is used to eliminate the artificial materials such as remaining air trapped inside the NOA. It is important to prevent the unwanted polymerization.

4.1.4 Experimental Setup for Characterizing SWWs

The production of an SWW between two opposing MMFs is shown in Fig. 4.2. The laser beam is guided by an MMF (e.g. illuminating Fiber) to the resin (e.g. NOA 68). It starts the polymerization process and thus, forms the SWW. The SWW carries the laser beam to the other MMF (e.g. collector fiber). The beam reaches the PM (power meter) by the collector MMF and the PO (power output) from the PM is obtained. At the final step, the heater is employed and the POs are recorded.

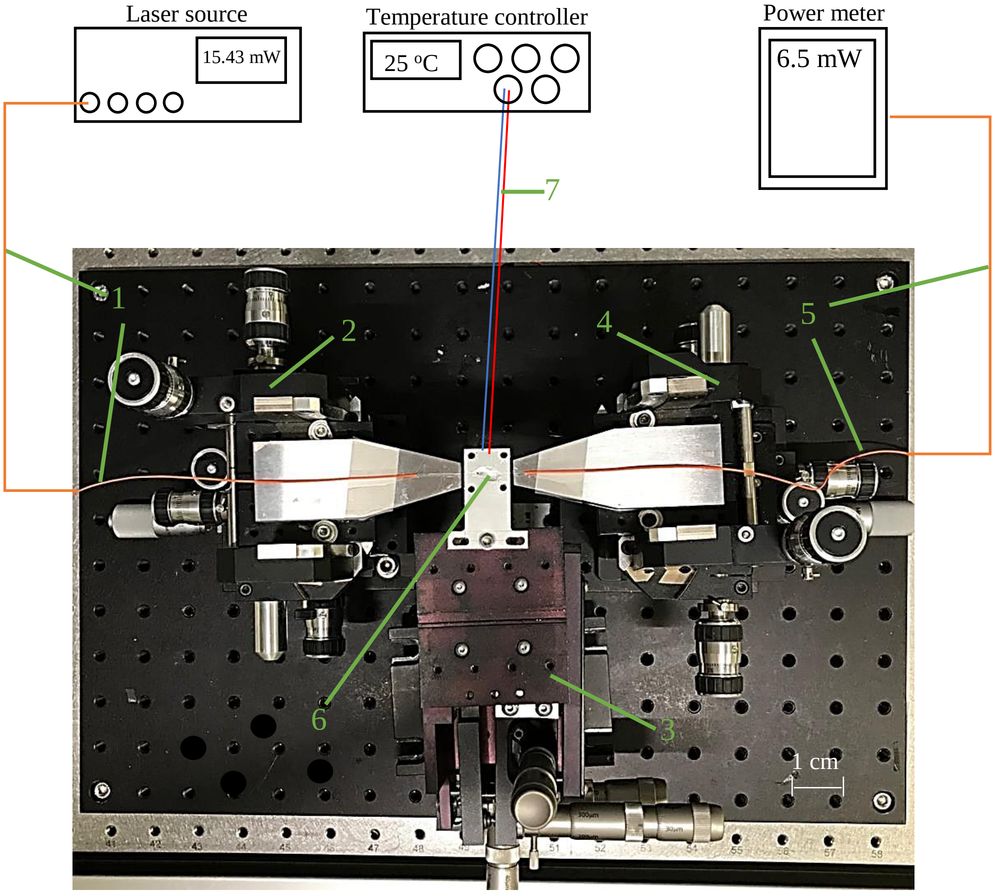

Figure 4.2 Overview of the SWW experimental setup. 1) Illuminating fiber is an MMF that is connected to the laser source. 2), 3), and 4) are 5-axis stages. 5) Collector fiber is an MMF that is connected to the PM. 6) Aluminum plate where SWW was created, the thermal element and the Peltier element are attached to (see Fig. 4.4 for further details), 7) are the cables that connect the T controller and the sensor and the Peltier element.

SWW formation: In the first step, two MMFs are taken and their jackets and claddings are peeled off about 5 cm from the offsets by a special stripping tool (Ripley Cromwell). The residues from claddings are washed off thoroughly by a chemical, isopropanol and then fibers are cleaved (Ilsintech Fiber Cleaver (MAX CI-03)). The fibers exhibit the best optical performance after these processes. Secondly, illuminating fiber’s FC/PC connector is plugged into the Thorlabs' 4-Channel Fiber-Coupled Laser Source (MCLS1-638, Thorlabs, Newton, USA) which possess 638 nm wavelength at 15 mW output power. The collector fiber is connected to a PM (PM200, Thorlabs, Newton, USA). Fibers are fixed and positioned across to each other with a small distance apart on a 19 mm by 19 mm aluminum plate as shown in Fig. 4.2.

The alignment of fibers is made with the help of a ZEISS SteREO Discovery.V8 microscope and three multi-axis high precision stages until the PM shows the maximum PO at the butt coupling position of the fibers as indicated in Fig. 4.3a. Our resin, NOA 68 is applied onto the butt coupled fibers in the third step. The fourth step is to separate the fibers with a defined gap size of ~750 µm, realign them, and obtain the maximum possible PO value from the PM again as shown in Fig. 4.3b.

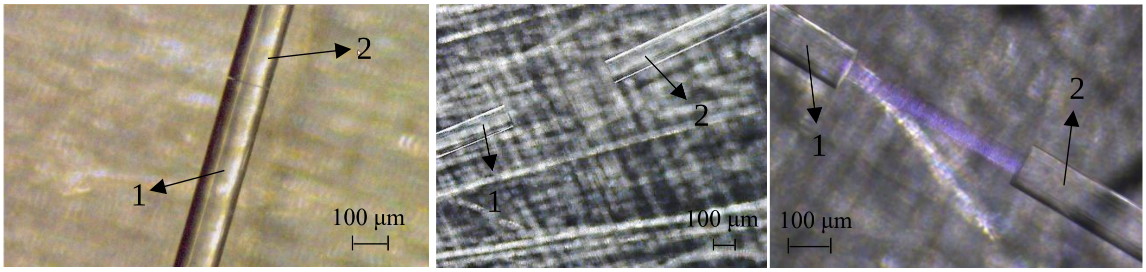

(a) (b) (c)

Figure 4.3 Steps of the SWW formation process. Fibers 1 and 2 are the illuminating and collector fibers, respectively. (a) Butt coupled MMFs so that laser beam transits from one fiber to another with maximum possible transmission, (b) Fibers are separated by a certain distance and (c) SWW is formed by 406 nm laser beam.

In the fifth step, the NOA 68 will be cured using a 406 nm laser beam (MCLS1-406, Thorlabs, Newton, USA) which has around 5.45 mW output power and forms the SWW as shown in Fig. 4.3c. The formation takes place even less than 1 s. During the curing process the transmitted power is monitored continuously. This writing process is stopped as the peak before the transmission starts decreasing. At this point, the surrounding NOA 68 is still liquid. This liquid is not stable and might cause unwanted fluctuations in the PO. Therefore, in the final step, it is cured externally by a 254 nm UV lamp with 1.8 mW/cm^2 (40-VL-208 G, Bio-Budget, Krefeld, Germany). This lamp can be aligned 2 cm away from the NOA. 5-minute curing at this distance would be enough to make a robust cladding around the SWW. After obtaining an SWW, the heater is turned on and heats up the sample from 25 ^{o}C to 60 ^{o}C and then 60 ^{o}C to 25 ^{o}C in the reverse direction by 5 ^{o}C increments (see Fig. 4.4) when it reached the desirable. The experiment is repeated at least 3 times and the POs are recorded for each temperature.

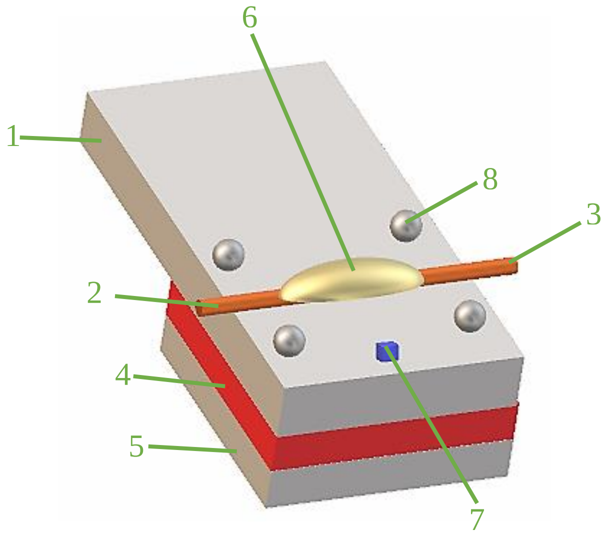

Figure 4.4 Setup for characterizing the response of the SWW after changing the temperature. 1) Aluminum plate, 2) and 3) are the illuminating and collector fibers, respectively, 4) is the Peltier element (e.g. heater) which is located under the aluminum plate, 5) Supportive aluminum plate, 6) NOA 68, 7) The temperature sensor, and 8) are the screws which connect the upper and the lower aluminum plates which holds the Peltier element still. Here is the place where SWW is formed and it is heated via Peltier element.

4.2 Experimental Setup to Determine the RI of the SWW

The setup shown in Fig. 4.5 was placed onto the aluminum plate. First, the illuminating fiber is placed on the N-BK7 glass and the collector fiber was placed on the other side of the sample holder. The fibers got aligned across to each other as shown in Fig. 4.6a. A 638 nm laser beam is utilized to make the alignment. It is accomplished when the PM shows the maximum PO that is much weaker than the one in the formation of the SWW experiment because there is no contact between the fibers. It is seen that there is the glass of the sample holder which causes the laser beam to undergo divergence. Therefore, the losses are higher (See Fig. 4.6b). NOA 68 is poured to the place where the sample holder and the reference glass intersect in the second step of the experiment and then the SWW is formed by the 406 nm wavelength laser beam shown in Fig. 4.6b in which high reflection is seen and it indicates the reason why the PO for the curing process is low.

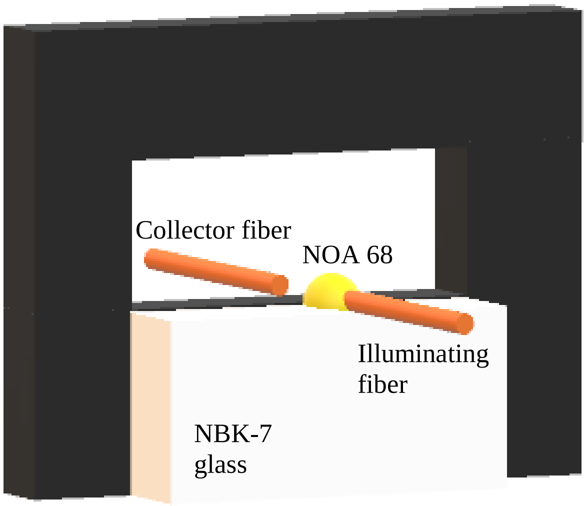

Figure 4.5 Sample preparation for RIPM. SWW is made in this setup. At the end, fibers are removed, the setup is inserted into RIPM, the outcomes are processed via a software and the RIPs of the SWW are obtained.

Nevertheless, the intensity of the beam is sufficient to cure NOA 68. It should be noted that this waveguide’s formation is required to be made perpendicular to the holder as shown in Fig. 4.6c and d. The experiment of the SWW formation is repeated to offer multiple sample which can be used for the RI measurement (see Fig. 4.6.d). Thereby, there is an opportunity to obtain the results of many SWWs from the RIPM.

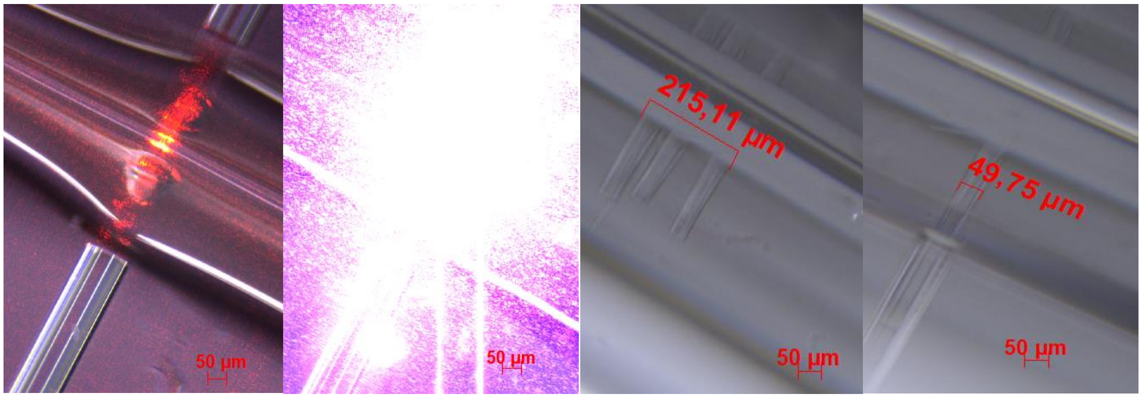

a) **b)** **c)** **d)**

Figure 4.6 The steps of the sample preparation for RIPM. a) The fibers are aligned, b) SWW formation by 406 nm wavelength laser, c) SWW is formed, and d) The experiment is repeated and more SWWs are produced. Illuminating and collector fibers are located at the bottoms and the tops of the pictures.

Now, the sample is ready to be examined in the RIPM. At the beginning, the 633 nm laser beam in the index profilometer is focused onto the area and scans it thoroughly in the x-y direction. This process occurs step by step. The steps were chosen in our experiment as 1µm for both of the directions. The laser beam passes through the objective, then the waveguide and finally reaches the photodiode from the side of the reference glass. The aperture stop plays a significant role to provide better performance for all the

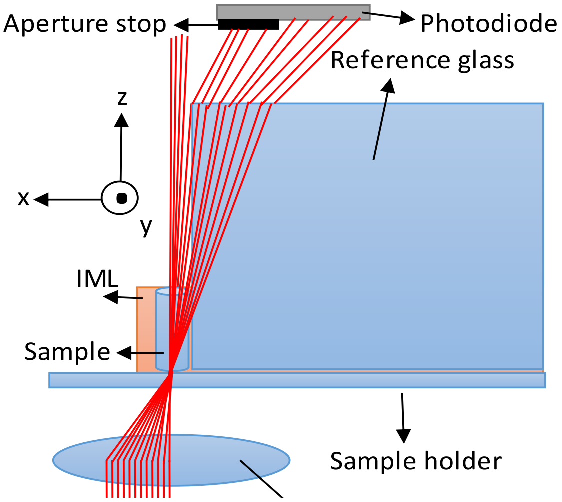

Figure 4.7 Overview of RIPM setup. The laser beam is focused on the sample, refracted toward the reference glass and captured by a photodetector at the end. RI is measured by the obtained data.

measurements. The correlation between the power of light at the detector and the RI is established in the last step and as result, a false color image is obtained which is formed according to the RIs of the references and the waveguide as shown in Fig. 4.8.

Dark blue and red colors represent the lowest and the highest RIs, respectively. The RI of any point in the picture can be found after the areas of the references that are glass block and IML are calculated and defined in the picture.

The measured for calculating the RIs should be the same for each measurement by different temperatures. Otherwise, the references will not have the same values at different temperatures and the changes between results might not exhibit correlational behavior. It changes the results significantly since the RI change is as small as 10^{-4}.

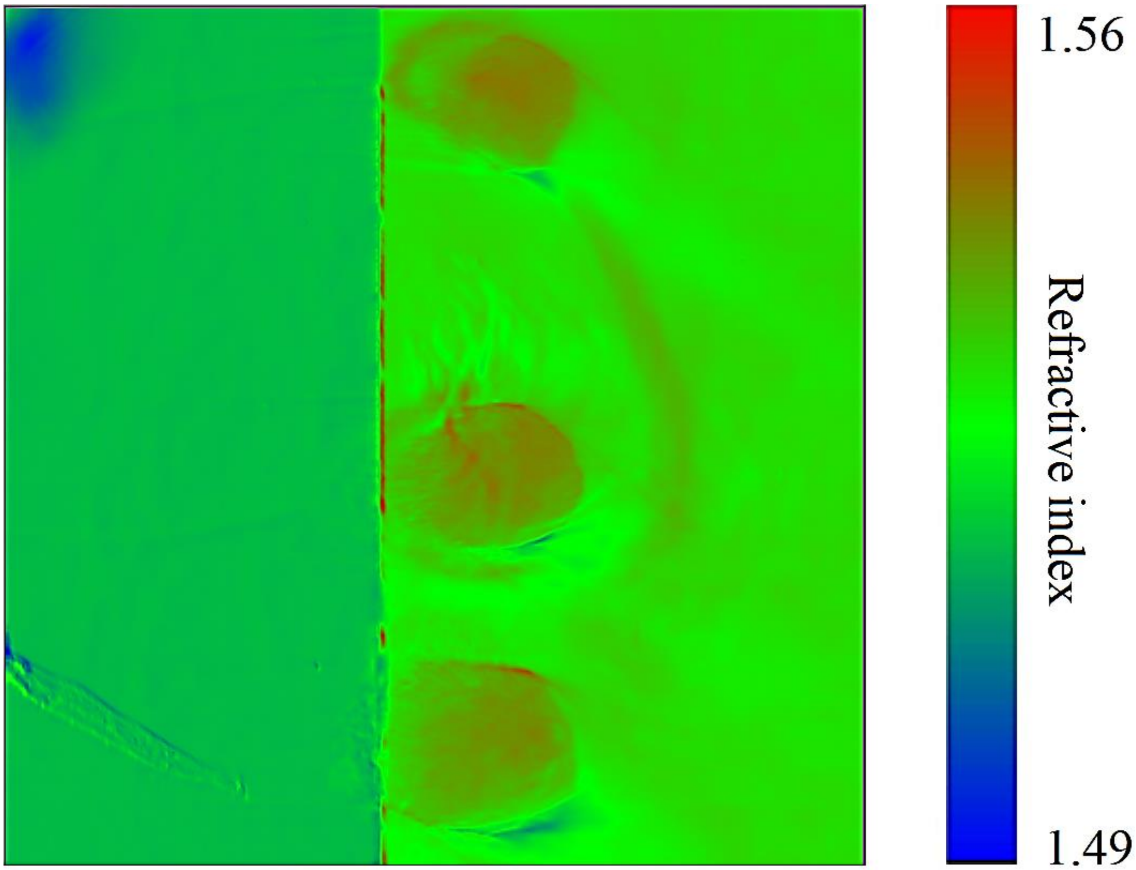

Figure 4.8 The picture of the RIPs of the SWW samples from the experiment shown in Fig. 4.6.d obtained from the RIPM. The 3 SWWs are located in the red and circular regions.

4.3 RIP of the Waveguide

The RIPs of the SWW are found for the heating and the cooling from 25 ^{o}C to 60 ^{o}C. If g is modified in the Eq. 2.1 for the GRIN MMF and is rewritten [72] it would be:

$$g = 2 - \frac{12}{5}\Delta \tag{4.1}$$

The RIPs of the SWW for the heating and the cooling processes can be simulated by importing the received data from the experiments and using the Eq. 4.1 in a MATLAB script file.

Chapter 5: Results and Discussion

In this chapter, the results from the experiments and the simulations of the study are presented, discussed, and compared. The correlations between them and also, between the previous research studies will be established. The analytical analysis made for the results is supported by the data that are obtained from the pictures, graphs, tables, etc.

5.1 Thermal Distribution through the SWW

The heater withdraws the maximum possible power from the power supply when it heats up the waveguide and the surrounding air. Thus, the heater increases the temperature of the waveguide as fast as possible. The heating process takes place swiftly, that it can be assumed that the heating was done before the measured data were noticed.

Table 5.1: The temperatures at the sensor (T_S) and the center of SWW (T_{SWW}) during the heating of the SWW. t is the time for the heat flow to reach the temperature of SWW. SWW is heated up from 25 ^oC to 60 ^oC.

T_S (^oC)	T_{sww} (^oC)	t(s)
26.463	25	1.15
31.423	30	0.83
36.430	35	0.83
41.400	40	0.81
46.385	45	0.81
51.370	50	0.93
56.320	55	0.79
61.28	60	0.8

On the other hand, the power supply stops providing the electrical energy to the heater during the cooling. Therefore, there is only one heat source left which changing the heat energy of the materials. This process does not need any electrical heating source and occurs much slower than the heating. The cooling takes place slower than 1.76 s which is more than 2 times slower than the heating as shown in Table 5.2.

Table 5.2: The temperatures at the sensor (T_S) and the center of the SWW (T_{SWW}) while cooling. t is the time for the heat flow to reach the temperature of the SWW. The SWW is cooled up from 60 ^{o}C to 25 ^{o}C.

$T_s(^{o}C)$	$T_{sww}(^{o}C)$	t(s)
56.320	55	1.76
51.370	50	1.77
46.385	45	1.78
41.400	40	1.78
36.430	35	1.78
31.423	30	1.79
26.463	25	1.79

As seen in the tables, there is a temperature difference between the heater and the SWW in the range of 1.320 to 1.463 ^{o}C. This approximation made in the simulation helps us to predict the right temperature for the SWW and thus, we obtain more accurate results.

The results (e.g. ≥ 0.79 s and ≥ 1.76 s) of the heating and cooling processes showed that the waiting time for the heating and the cooling are not significant as it was observed in the experiment.

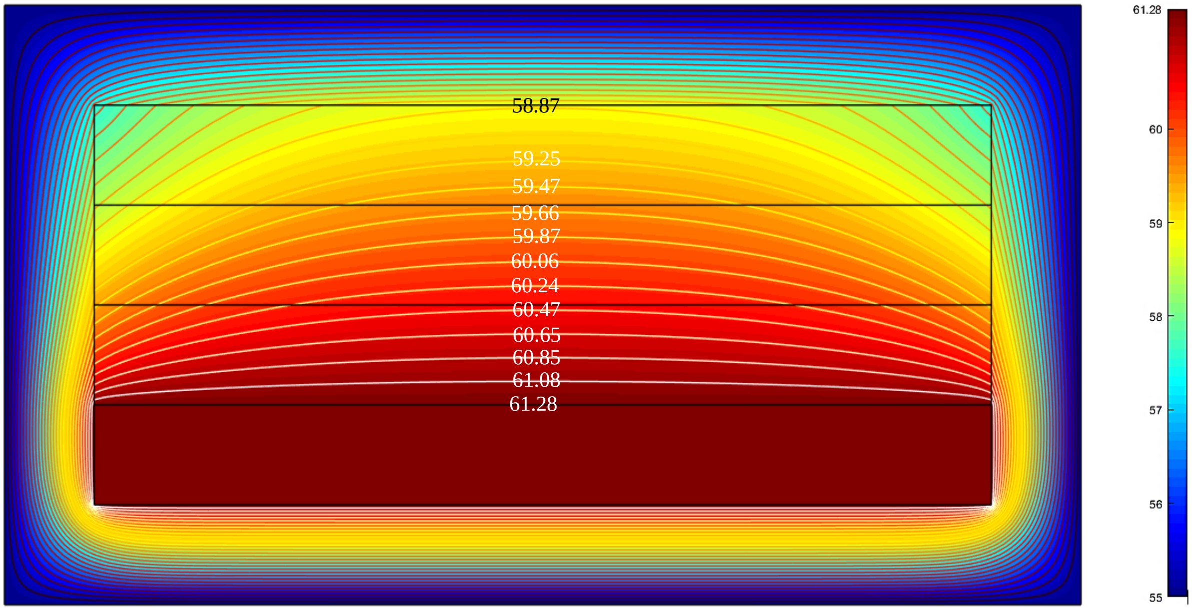

Figure 5.1 Contour maps of the temperature distribution along a cut line in the middle of the waveguide when the heater was at the maximum temperature of 61.28 ^{o}C.

The temperatures along the contour line is perpendicular to the z-axes obtained from the mid-point of the microheater. The dark red color and the dark blue color in the color scheme indicate the highest and the lowest temperatures, respectively.

5.2 Transmission Measurements of SWW

5.2.1 Curing Times

The internal curing (INC) of the SWW and the external curing (EXC) of the NOA around the SWW are the processes where the laser beam is highly attenuated. The most appropriate times should be chosen for them in order to build a low attenuated structure.

The internal curing: This process has to be meticulously observed. The PO value for 406 nm beam is correlated to the PO for 638 nm beam. The process was observed for 60 minutes and illustrated as shown in Fig. 5.2. The PO at the beginning of this process was 1.92 mW (red dot in Fig. 5.2) and the black dot shows the maximum value 2.44 mW.

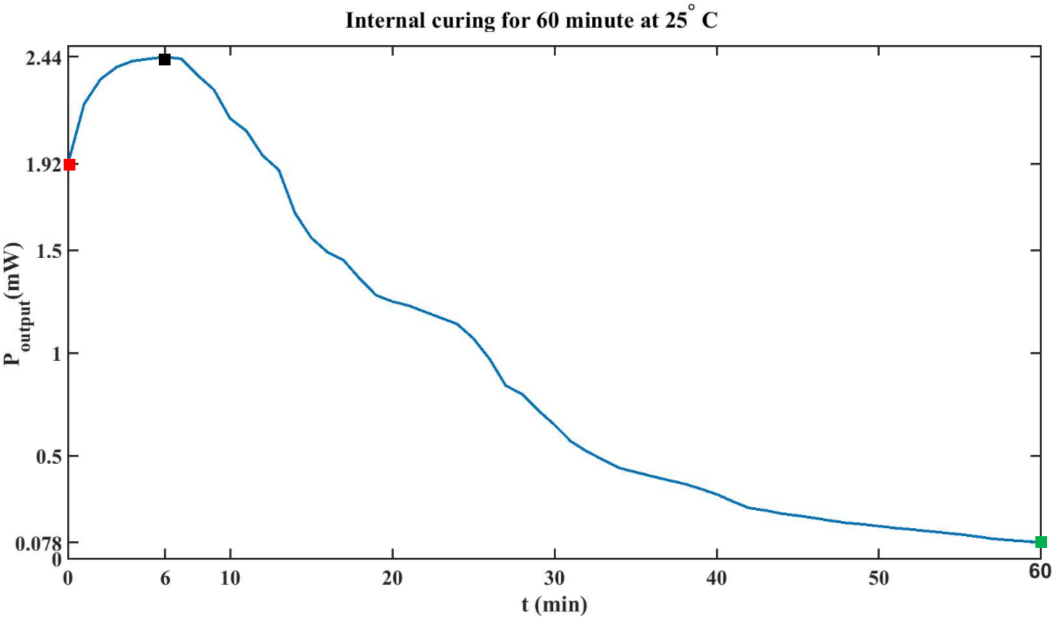

Figure 5.2 INC for 60 minutes at 25 ºC. PO increases at the beginning of INC until the formations of the small channels that bridge the illuminating and collector fibers are finished. It decreases due to the excessive number of the artificial channels formed around the fibers. The laser beam diffracts out due to them.

Here, we made a detailed investigation of the beam diffraction for 60 minutes around the SWW. The laser beam diffracts from the sides of the collector fiber, even in the very first seconds. This fact is picturized in Fig. 5.3a.

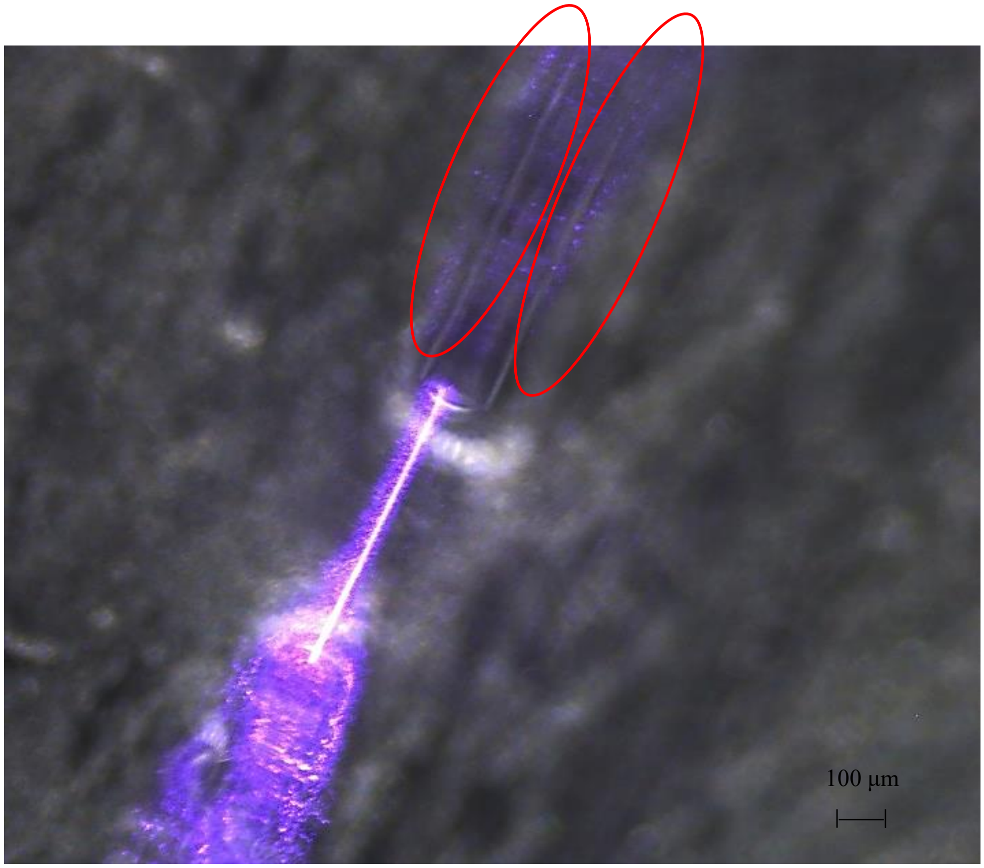

Figure 5.3a Laser beam diffraction just after the laser source turned on (e.g. 1 second later). The lost is seen at the very early stage of the INC process. Nevertheless, the transmission is in an increasing trend because more bridging optical channels between the fibers are added.

This leakage gets bigger constantly over time and forms more small channels around the SWW and the fibers. The scale of the laser beam scattering can be observed even a minute later as shown in Fig. 5.3b.

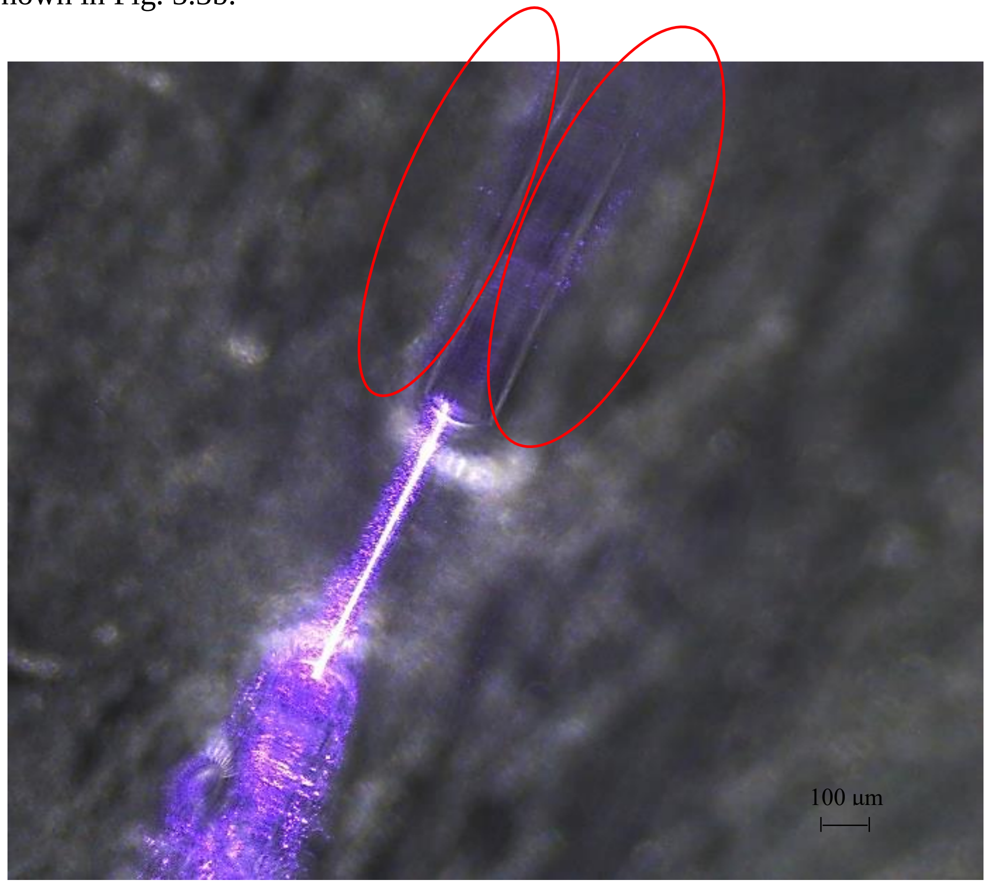

Figure 5.3b Laser beam diffraction, 1 minute after starting the curing. The amount of diffraction around the collector fiber increases constantly. However, they have not reached to the point where the PO starts decreasing

The diffraction causes a loss in the PO. But the number of the bridging optical channels formed between the fibers is much greater in the terms of quantity than the artificial ones around the collector fiber. Therefore, in the beginning, there is a temporary gain due to those bridging optical channels between the fibers that increase the PO. It is shown in Fig. 5.2 that the PO increases as high as 2.44 mW. It reaches this value 6 minutes after the process was started. After this point, the loss due to the small channels which surround the collector fiber overweighs the gain and thus, the PO starts decreasing.

Fig. 5.3c and d depict the fact that the leakage gets bigger constantly and spreads everywhere around the illuminating and collector fibers, and the SWW.

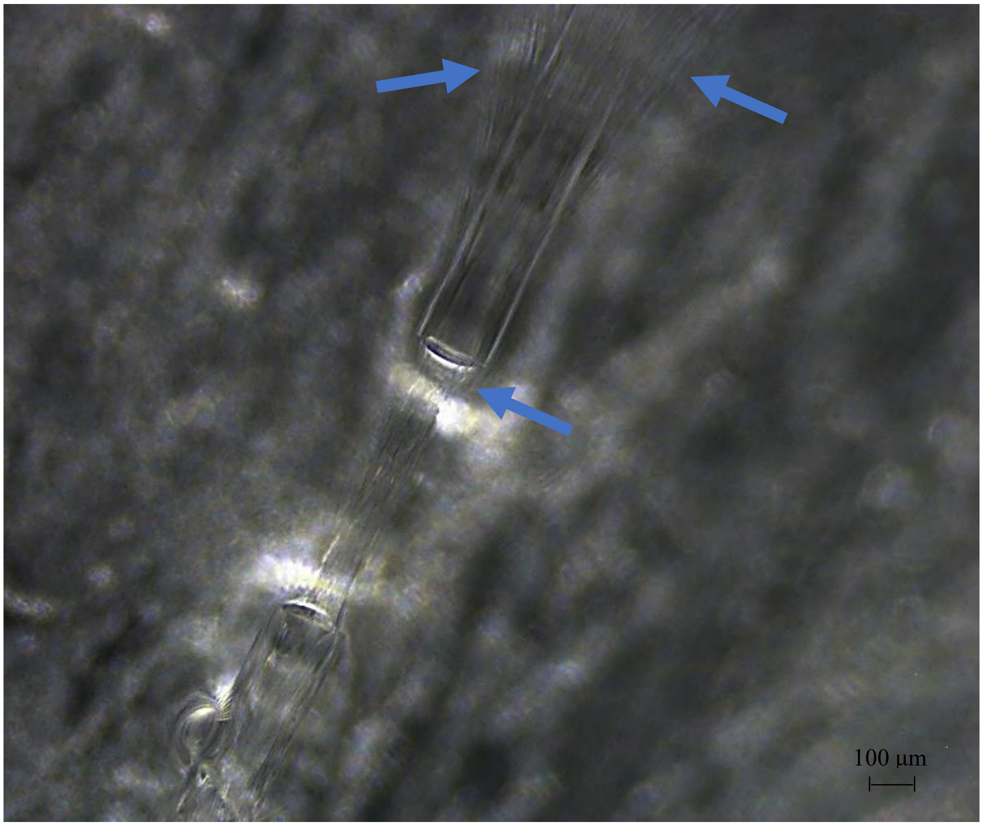

Figure 5.3c Laser beam diffraction, 30 minutes after the beginning. The small artificial channels are around the collector fiber and the SWW and thus, the attenuation is very high. Therefore, the SWW is not suitable to be used.

At the end of 60-minute INC, the laser beam diffracts out all the places and there is very little left which is guided through SWW. Therefore, PO decreases as little as 0.078 mW (see Fig. 5.2). The channels exist even around the SWW and the illuminating fiber. Moreover, the ones which are formed by the back-reflecting beam, are even observable shown in Fig. 5.3d.

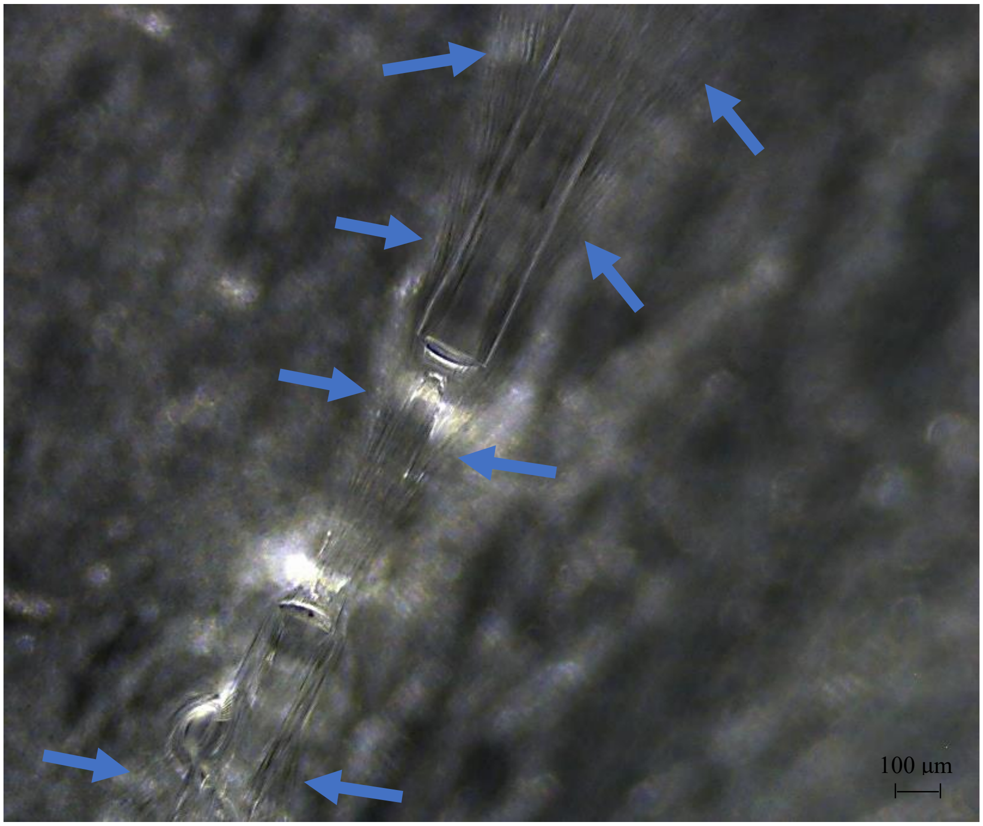

Figure 5.3d Laser beam diffraction, 60 minutes later. The diffraction of the laser beam is at the maximum rate due to channels formed everywhere around the illuminating, the SWW, and the collector fibers.

The external curing (EXC): In the previous section (INC), a certain time is defined for the curing where SWW has the optimum transmission. However, a definite point does not exist for the EXC. It should be conducted until the waveguide possesses a vigorous structure. To find it out, the EXC was made on the NOA 68 material separately on a different plate for 1, 3, 5, 10, and 15 minutes, consecutively. The outcomes showed that a 5-minute EXC is enough to obtain a strong waveguide. Of course, longer EXC will provide more robust structure. But it will be associated with high attenuation. It is seen in Fig. 5.4 that the intensity decreases to 0.64 percent at the end of 30-minute EXC.

The EXC causes loss in the waveguide remarkably so that it might decrease the PO as high as 19 percent (see Fig. 5.4).

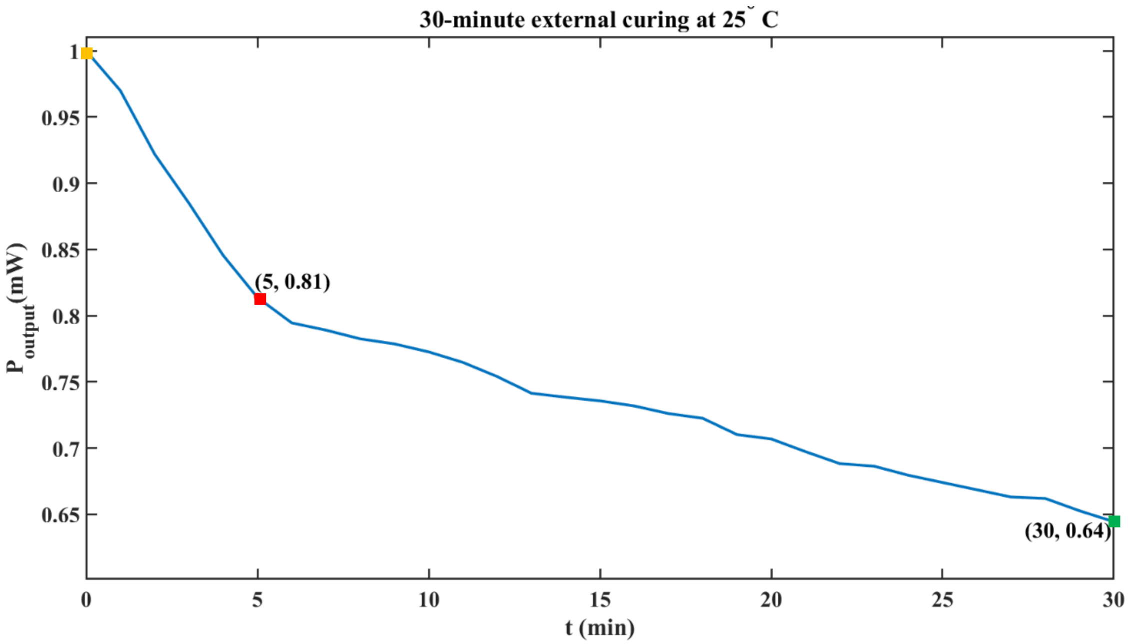

Figure 5.4 EXC of the SWW for 30 minutes at 25 °C. Orange dot shows the value obtained just after the INC, red dot indicates the value where the waveguide has a robust structure which occurs 5 minutes later. At the end of the experiment, the PO drops to as low as 0.64 that is shown by the green dot.

As a result, there are no certain times that determine when the maximum possible transmission of SWW is achieved. But they can be easily found out for each experiment when they can be acquired. The ideal curing times of INT and EXC are the time when the PO peaks and 5 minutes after the beginning of the curing, respectively.

5.2.2 Thickness of SWW by Temperature and during Curing

The change in the thickness of SWW is not remarkable to be observed when it is heated. This fact is also similar to the results of NOA 61 and 81 where they are as small as <10 nm as van Gastel et al. indicates [73].

As it is stated before in section 5.2.1 that the INC forms the SWW swiftly. This fact can be seen in Fig. 5.5. Also, the figure shows that the SWW which is needed is obtained at the very beginning of the INC process. Furthermore, there is a correlation between the PO during the INC and the thickness. The bridging small optical channels are formed mostly between the fibers. Therefore, the SWW does not get thicker until the PO peaks (see the red circle in Fig. 5.5). Hence, the slope of the line in Fig. 5.5 is very small. After this point, the focusing effect of the fiber get weaker, thus, the PO decreases exponentially as much as the magnitude of the slope.

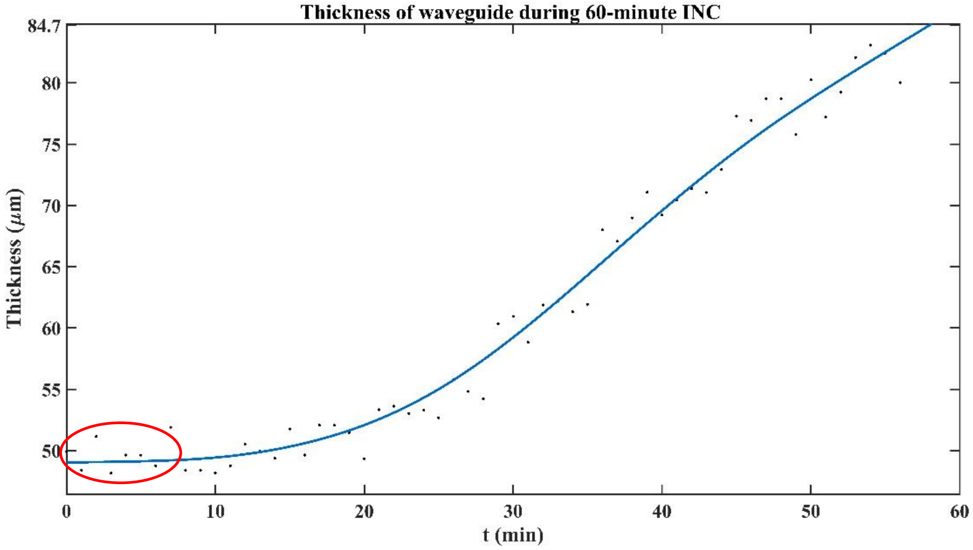

Figure 5.5 Thickness of the SWW during the 60-minute INC. The slope of the line and the PO has a negative correlation after the PO peaks. The red circle shows the area where more channels are added to the SWW that help guiding the beam. Moreover, it does change the thickness of the SWW and cause the attenuation.

The EXC does not affect the thickness of the SWW because the intensity of the UV laser beam is well distributed throughout the NOA.

This is another factor besides INC and EXC that causes the loss in the PO.

5.2.3 Temperature Effect on Power Output Intensity

The POs displayed on the PM have a positive correlation with temperature. The experiments are repeated at least 6 times or more to observe it. The outcomes at the beginning of the experiments are not as accurate as compared to the end. Because the prepared SWW still undergoes the polymerization by the 638 nm laser beam. The photopolymer media also support the formation of the SWW at 638 nm [15]. The polymerization influences the PO significantly. Therefore, the first cycles cannot illustrate the temperature effect on the PO properly (see Fig. 5.6). The polymerizability of the beam gets faded as time passes, thus, the change in the PO between each cycle decreases as shown in Fig. 5.6. Therefore, the outcomes become more precise. The further experiments showed that the PO difference between the cycles becomes even 0. Because the polymerization process is accomplished.

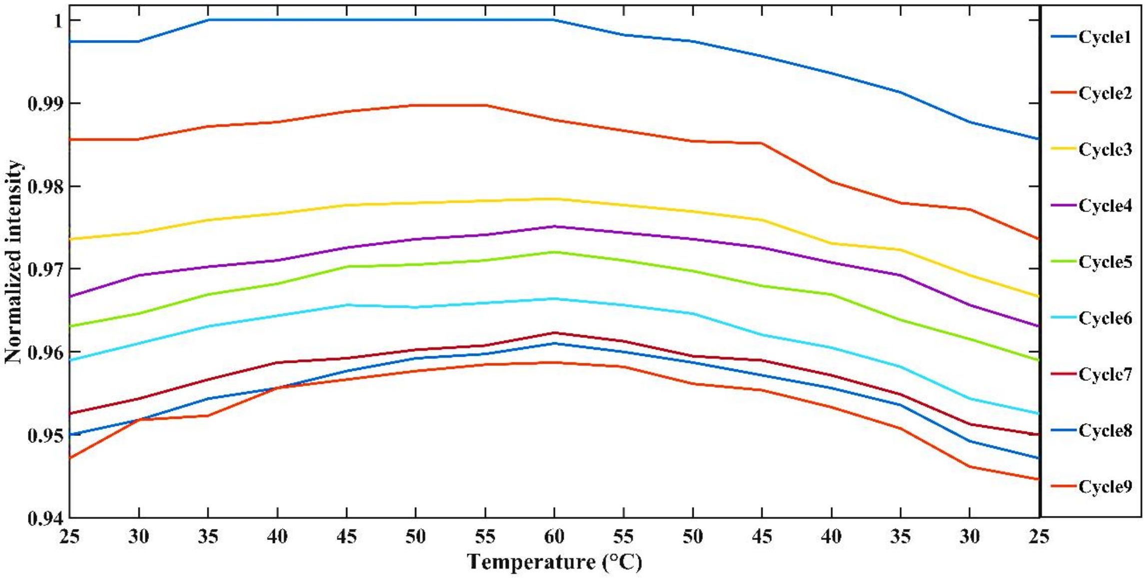

Figure 5.6 Temperature effect on the transmission of the 638 nm laser beam guided by SWW. The SWW still undergoes a polymerization process at the beginning. Therefore, temperature dependency is not seen clearly (see cycle 1). It has a stable intensity after 6 cycles where temperature effect can be examined (see cycle 7, 8, and 9)

5.2.4 Temperature Effect on SWW at Different Intensities

In this step, the PO change by the temperature for different intensities/currents is examined. The PO was decreased from 100 % to 20 % by 20 % increment as illustrated in Fig. 5.7. Temperature effect on the PO has a positive correlation with the power intensity. However, the effect becomes very small compared to the intensities. The normalized deviations are also very small at all the intensities, so that they cannot be observed.

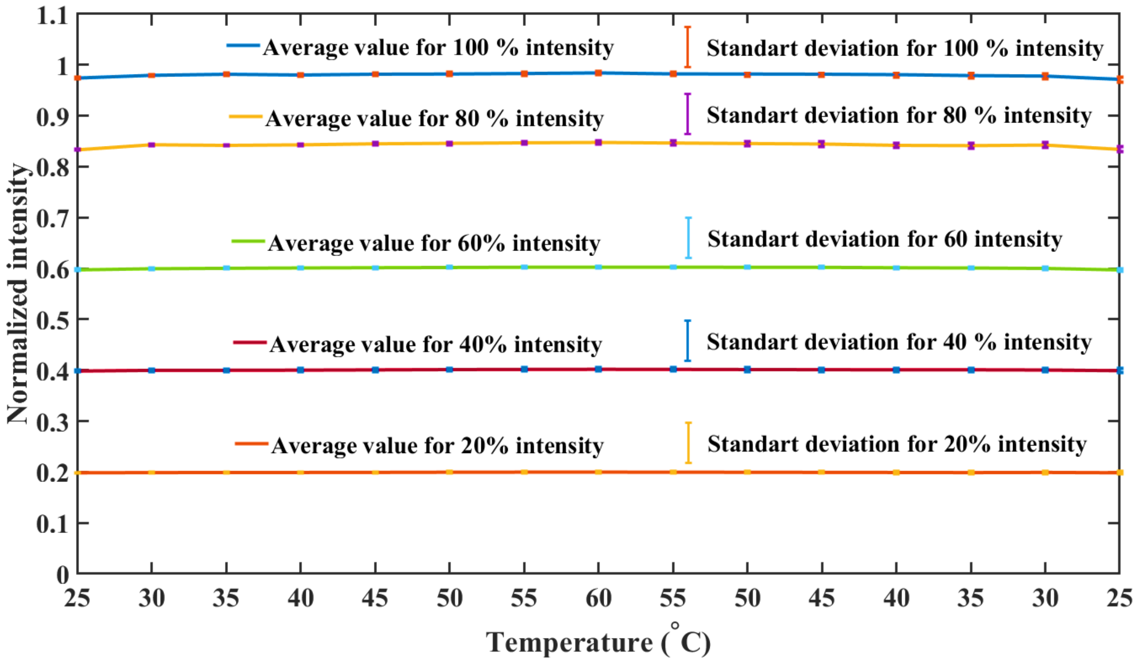

Figure 5.7 Temperature effect on the transmission of the 638 nm laser beam guided by SWW at the different intensities. The results do not show a significant difference by decreasing intensity. The fraction of the transmitted light stays same.

As a result, after all the processes accomplished so far, the INC and EXC are the main factors that cause the change in the transmission as depicted in Fig. 5.8. The first process where the fibers are butt-coupled shows there are coupling losses although the two fibers were coupled directly with each other. There is around 15% power loss during this process. Most of the loss is regained by adding the resin (NOA 68). The loss drops to less than 3 percent after this process due to the higher refractive index and the change of the NA, respectively. Before the INC, the fibers are taken apart 500 μm that causes the loss most among the processes, it is approximately 43%. However, the INC compensates the loss because it provides a better guiding to the beam, and hence, normalized intensity increases up to 87 %. Subsequently, after the EXC process, it decreases the intensity to 0.837. Finally, it increases to 84.8 % after heating of the SWW. It is emphasized that the values in Fig. 5.8 are the optimum values out of the experiments. It was observed that the loss in the intensity level after the processes decreases to as low as 80 %.

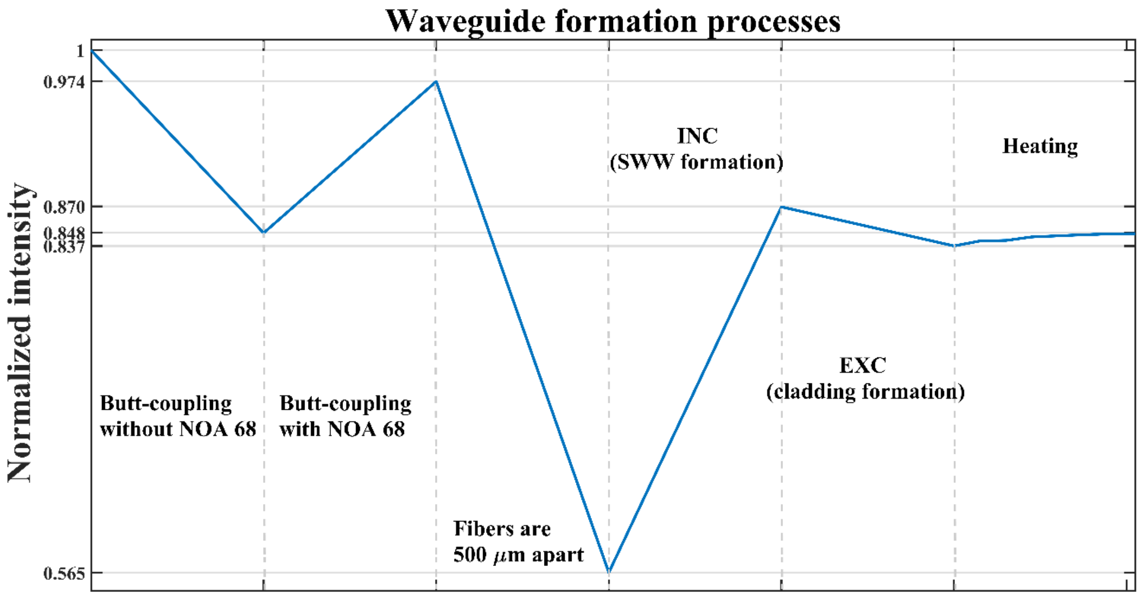

Figure 5.8 Waveguide formation processes. The figure shows all the processes with their normalized intensities throughout the waveguide formation. The normalized intensity decreases to 83.7 % when all the formation processes of the waveguide is completed. It increases to 84.8 % after the heating to 60 °C

5.3 SWW Measurements in RIPM

5.3.1 RIs of the Waveguide

The parameters in Table 5.3 are obtained from the RIPM software. The RI of the uncured NOA 68 was 1.514. The RI change has a correlation with the intensity of the curing beam [74]. Therefore, the increase of the RI for the SWW is higher due to the intense laser beam. Another difference is the RI change of the SWW and the cladding during heating. We observe from the table that the RIs for core and cladding both are in the decreasing trend. The key point which makes the SWW stable for the temperature, is that the change in the RI of the cladding is ~2.2 times greater than the RI of the SWW. Here, there is a negative correlation between the temperature and the RI. The RI of the cladding is expected to decrease less because its temperature is less than the core (see Fig. 5.1). This would be valid if we assume that the SWW and the cured NOA 68 have the same or similar structures [16]. The methods how the materials are cured are crucial in the modulations of RIs of the core and the cladding. The NOA 68 is cured by a relatively lower intensive light that forms a feeble and less dense structure. Moreover, the SWW is cured by a higher intensive laser beam that makes a robust and denser formation. This makes the biggest change in the RIs. The confinement factor (see section 2.1) shows us the reason of the higher transmission through the SWW during the heating. It increases especially from 25 ^oC to 30 ^oC. The values of confinement factor confirm the transmission results obtained from the experiments as depicted in Fig. 5.7.

Table 5.3 SWW parameters obtained from the RIPM and the calculations.

T(^oC)	n_{sww}	$n_{cladding}$	D	Γ
25	1.51845	1.51767	23.93505	0.9965
30	1.51826	1.51710	29.13062	0.9976
35	1.51819	1.51690	30.80174	0.9979
40	1.51808	1.51674	31.42124	0.9980
45	1.51800	1.5165	32.72522	0.9981
50	1.51786	1.51632	33.60942	0.9982
55	1.51777	1.51611	34.85628	0.9984
60	1.51767	1.51590	36.05471	0.9985

5.3.2 RIP of the SWW

Δ and g parameters are calculated by Eq. (2.1) and (2.2) as shown in Table 5.4.

Table 5.4 The parameters used in MATLAB to plot the graph for the RIP of SWW

T(^oC)	Δ	g
25	0.000128	1.99969
30	0.000190	1.99954
35	0.000212	1.99949
40	0.000221	1.99947
45	0.000240	1.99942
50	0.000253	1.99939
55	0.000272	1.99935
60	0.000291	1.99930

MATLAB solves the Eq. (2.1) with the help of the parameters in Table 5.4 and plots the curves in Fig. 5.9. The outcomes show that the SWW possesses a non-homogeneous RI distribution that is similar to the GRIN fiber.

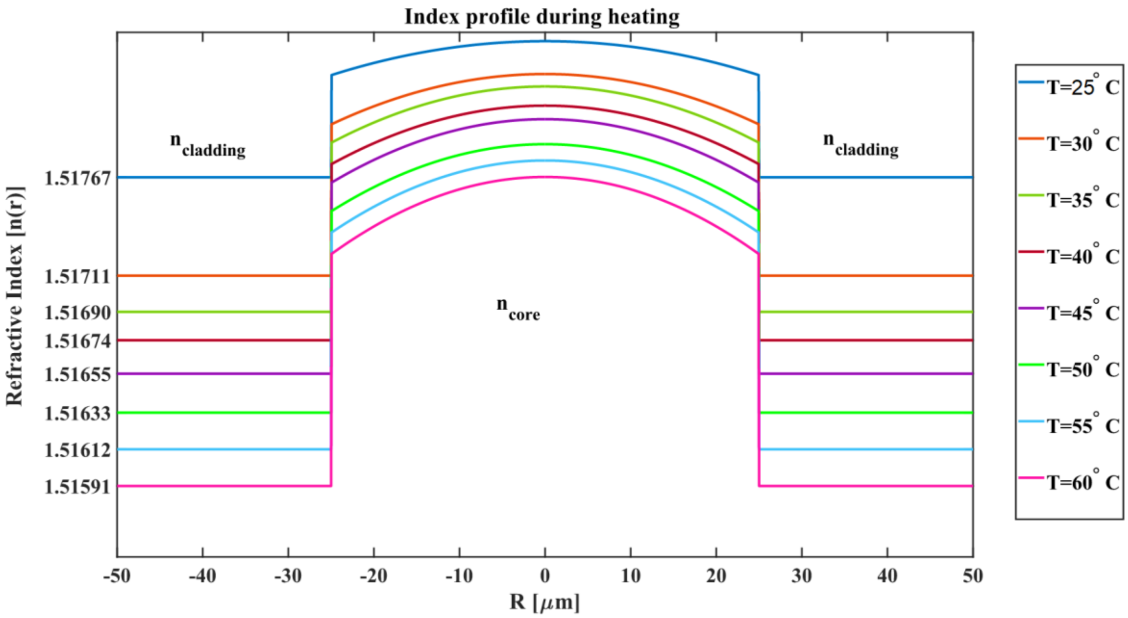

Figure 5.9 RIPs of the SWW during the heating from 25 °C to 60 °C across the waveguide (e.g. core and cladding). RIs of the cladding decreases about 2.2 times faster by the temperature.

Also, the fact can be experimentally proved by the RIPM as shown in Fig. 5.10. The picture only shows the experimental result of the RIP of SWW. The flat lines on the right and left sides belong to the RIs of N-BK7 glass and IML, repectively.

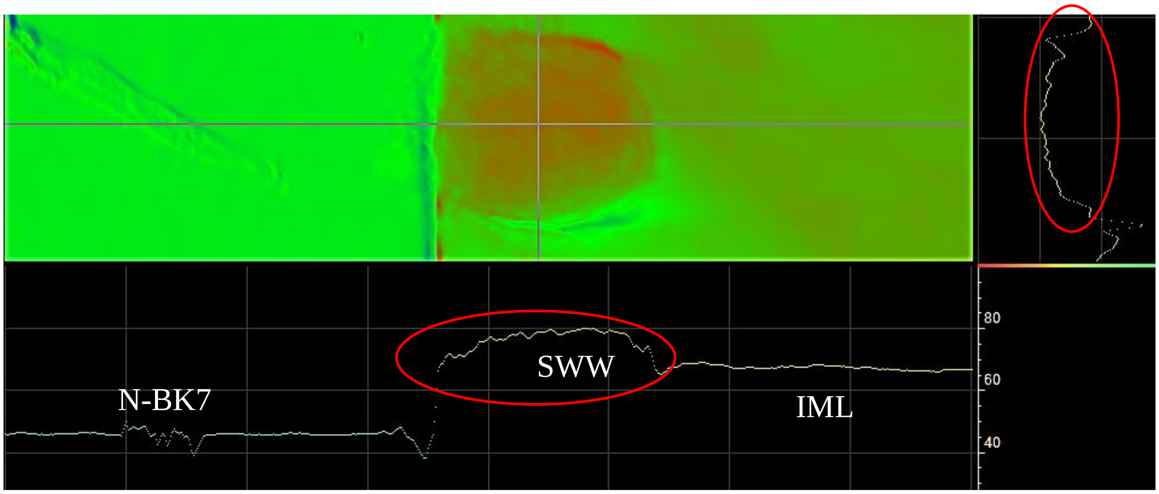

Figure 5.10 RIP of the SWW at 25 °C. The picture is processed by the software of the RIPM to measure the RIs changing by temperature. In the red circles, it is seen that the SWW has a similar RIP as in GRIN MMF.

As a result, the techniques used in this project to determine the RIP help us to understand the nature of the RIP of the SWW.

5.4 Optical Simulation of SWW

5.4.1 Transmission

The data can be obtained from the optical simulation about the reflection (R) and the absorption (A) of the waveguide besides the transmission (T) shown in Table 5.5. They show that the heating of the SWW has more influence on the transmission between 25 ^{o}C and 30 ^{o}C as it is seen in the experimental results. Also, it is the temperature interval where the beam is undergone the most absorption by the material.

Table 5.5 R, A, and T of the SWW by temperatures.

T (^{o}C)	T	R	A
25	0.99250	0.02899	0.0075010
30	0.99454	0.02464	0.0054532
35	0.99506	0.02373	0.0049410
40	0.99521	0.02357	0.0047893
45	0.99549	0.00236	0.0045027
50	0.99565	0.02443	0.0043479
55	0.99572	0.00283	0.0042808
60	0.99577	0.02784	0.0042804

The experimental and simulation results are plotted in a graph shown in Fig. 5.11. The graph shows that the temperature dependency of the PO is not remarkable after 40 ^{o}C. There is a little difference between the changes in the normalized intensities of the simulation and the experiment. Because of the special features of COMSOL such as boundary condition, the modes coupled to the cladding are eliminated. Therefore, the values from the optical simulation are higher.

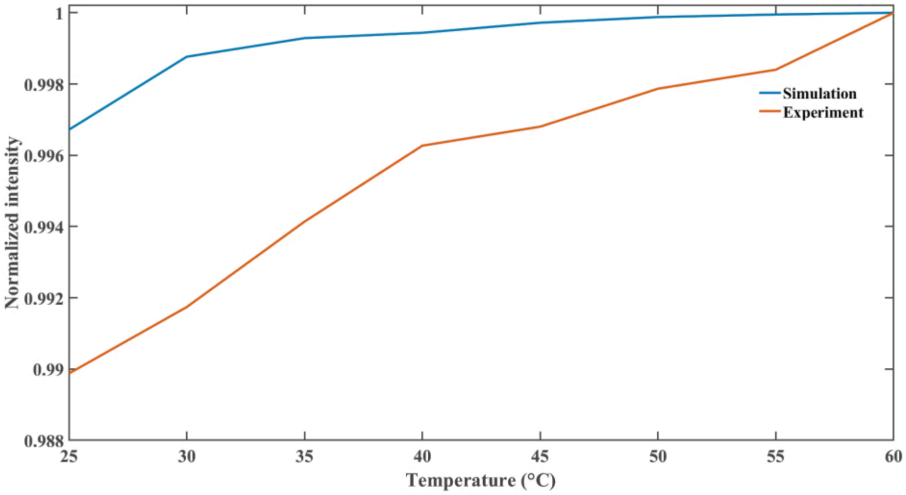

Figure 5.11 Experimental and simulation results of normalized intensity. Both of results show that the change in the intensity of the output beam is not significant.

5.4.1 Beam Profile

The temperature increases the NA and M of the SWW as shown in Table 5.6. This change is employed and the beam profile is illustrated in Fig. 5.12. The electrical fields of the TE and TM modes are $1.9 \cdot 10^5$ V/m and $1.83 \cdot 10^5$ V/m, respectively, the values are very close to each other at 25 ^{o}C. The temperature change affects the modes oppositely. Electric field in TE mode increases to $5.88 \cdot 10^5$ V/m at 60 ^{o}C while it drops to $1.57 \cdot 10^5$ V/m in TM modes. The change of electric field in TE modes is remarkable during the heating which is observed in Fig. 5.12c. Besides that, electric field in TM modes is slightly disturbed. Therefore, the deformation is barely seen in Fig. 5.12d.

Table 5.6 NA and M values of the SWW

NA	M
0.0243	8.95
0.0296	13.27
0.0313	14.83
0.0319	15.44
0.0332	16.75
0.0341	17.66
0.0354	19.00
0.0366	20.33

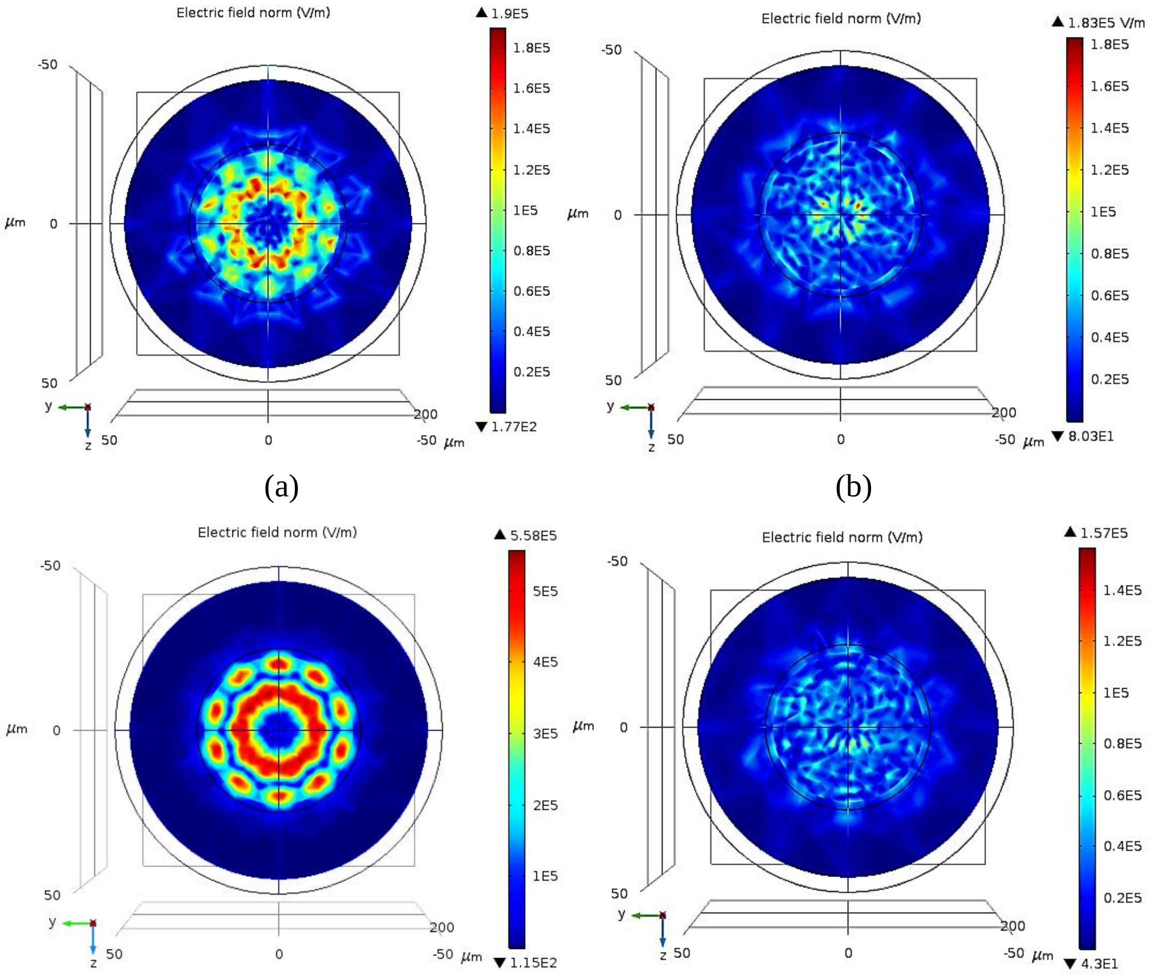

(a) (b)

(c) (d)

Figure 5.12 Optical fields of TE (b and d) and TM (a and c) modes of the waveguide at 25 ºC and 60 ºC, respectively. The deformation of the optical field of TM modes is not observable. However, there is a significant change in TE modes.

Chapter 6: Conclusions and Future Work

This study is aimed to make a comparative analysis of simulated and experimentally fabricated SWWs and their thermal behavior. This thesis has proposed the models to achieve the goal. The experimental data were obtained by using the resin NOA 68 and the theoretical models were implemented into the FEM-based software COMSOL. The models can be modified and easily utilized for different types of SWWs that undergo the polymerization process.

The first step to achieve the goal was a thermal simulation which showed a temperature difference between the temperature sensor and the temperature of the SWW of the used experimental setup. The values vary in the range of 1.320 to 1.463 ^{o}C for the temperatures from 25 ^{o}C to 60 ^{o}C. This simulation provided us the approximated values of the temperature measured by the sensor. Thus, the corresponding transmission for each temperature became more accurate. Also, the thermal simulation modeled for the SWW setup has a more stable structure and yield more precise results than the previous model developed by Suar et al. [16]. The model can be implemented utterly to the other SWW made from different types of NOAs, or polymer- and silica-based waveguides to get more accurate results. Subsequently, the detailed analysis about the transmission of the beam during the formation of the waveguide was made. They are concluded that the internal curing process should stop when the power output from the power meter peaks after starting the process and the optical transmission continuously increases. There is no certain time for it proposed because it is distinctive for each experiment and it varies between 2 to 7 minutes. It is found that the external curing decreases the transmission all the time. There is no certain peak point to stop the process for the internal curing. Here, 5-minute external curing time is enough to build a robust cladding. Here, the durations of curing times are determined with the findings from the experiment that is vital to possess an efficient waveguide. There are many curing times are suggested in the previous research studies [9, 12, 14, 15, etc.]. This analysis removed the blurriness in this field by the experimental findings and guide the scientists in establishing an efficient waveguide made out of NOAs.

All the factors that affect the transmission are gathered in a graph and the normalized intensity of the processes is showed. It is concluded that the normalized intensity decreases to 84.8 % after all the processes including heating. The outcomes from the experiments showed that this value decreases to as low as 80 %. To make the comparison of the experimental and simulation result, the refractive indices of the SWW and cladding were needed. A very distinguished and complicated SWW setup is built on the sample holder of the refractive index profilometer to find the refractive indices of the core and the cladding. The data are obtained after a long process on the device and its software. The processed data are utilized to make the simulation and plot the refractive index profiles for the temperatures from 25 ^{o}C to 60 ^{o}C. The experimental and the simulation results are compared and showed a corresponding behavior. Also, the factors in all curing processes that cause the loss in the SWW are gathered and made their comparisons. In addition, an optimum efficient and temperature resilient optical waveguide will be produced if the refractive index profile of the SWW is taken a base. Finally, the optical simulation is made with the help of the data obtained from refractive index profilometer and the results from the experiment of the fabricated SWW, and the simulation are compared. Furthermore, the beam profile is picturized with the data obtained that showed that there is a significant change of the electrical field in TE modes. Besides that, the deformation is little in TM modes. As a conclusion, they exhibit the similar behaviors. The model developed for this research can be implemented to the different types and the length of other adhesives such as NOA 61, 63, etc. It is suitable for SMF and MMF both. More accurate results can be obtained for optical simulation by using equation-based modelling in COMSOL if the equation of the curve of the SWW is made out of the data where the thicknesses of all the points on the SWW is measured. The effect of the temperature on the transmission in the SWW is not significant since it is very small. Therefore, it is not possible to utilize it as a temperature sensor. This confirms the finding of the investigation of Liu et al. [13].

REFERENCES

1. Zhu, C., Zhuang, Y., Zhang, B., Muhammad, R., Wang, P. P., & Huang, J. (2018). A miniaturized optical fiber tip high-temperature sensor based on concave-shaped Fabry–Perot cavity. IEEE Photonics Technology Letters, 31(1), 35-38.

2. Zhang, G., Yang, M., & Wang, M. (2013). Large temperature sensitivity of fiber-optic extrinsic Fabry–Perot interferometer based on polymer-filled glass capillary. Optical Fiber Technology, 19(6), 618-622.

3. Deng, M., Zhu, T., Rao, Y. J., & Li, H. (2008, November). Miniaturized fiber-optic Fabry-Perot interferometer for highly sensitive refractive index measurement. In 2008 1st Asia-Pacific Optical Fiber Sensors Conference (pp. 1-4). IEEE.

4. Xu, F., Lu, L., Lu, W., & Yu, B. (2013). In-line Fabry-Perot refractive index sensor based on microcavity. Chinese Optics Letters, 11(8), 082802.

5. Zhao, T., Gong, Y., Rao, Y., Wu, Y., Ran, Z., & Wu, H. (2011). Fiber-optic Fabry-Perot strain sensor based on graded-index multimode fiber. Chinese Optics Letters, 9(5), 050602.

6. G. K. B. Costa, P. M. P. Gouvêa, L. M. B. Soares, J. M. B. Pereira, F. Favero, A. M. B. Braga, P. Palffy-Muhoray, A. C. Bruno, and I. C. S. Carvalho, ‘‘Infiber Fabry–Pérot interferometer for strain and magnetic field sensing,’’ Opt. Express, vol. 24, no. 13, p. 14690, 2016.

7. Yamashita, K., Kitanobou, A., Ito, M., Fukuzawa, E., & Oe, K. (2008). Solid-state organic laser using self-written active waveguide with in-line Fabry–Pérot cavity. Applied Physics Letters, 92(14), 124.

8. Kwack, M. J., Kanda, M., Mikami, O., Yonemura, M., & Kagami, M. (2010). 180$^{\circ} $ Light Path Conversion Device With Tapered Self-Written Waveguide for Optical Interconnection. IEEE Photonics Technology Letters, 22(15), 1126-1128.

9. Malallah, R. E., Li, H., Kelly, D. P., Healy, J. J., & Sheridan, J. T. (2017). A review of hologram storage and self-written waveguides formation in photopolymer media. Polymers, 9(8), 337.

10. Anderson, A., & Peters, K. (2009). Finite element simulation of self-writing waveguide formation through photopolymerization. Journal of Lightwave Technology, 27(24), 5529-5536.

11. Missinne, J., Beri, S., Dash, M., Samal, S. K., Dubruel, P., Watté, J., & Van Steenberge, G. (2014). Curing kinetics of step-index and graded-index single mode polymer self-written waveguides. Optical Materials Express, 4(7), 1324-1335.

12. Günther, A., Petermann, A. B., Gleissner, U., Hanemann, T., Reithmeier, E., Rahlves, M., ... & Roth, B. (2015). Cladded self-written multimode step-index waveguides using a one-polymer approach. Optics Letters, 40(8), 1830-1833.

13. Liu, Z. D., Liu, B., Liu, J., Fu, Y., Wang, M., Wan, S. P., ... & Wu, Q. (2020). Sensing characteristics of fiber Fabry-Perot sensors based on polymer materials. IEEE Access, 8, 171316-171324.

14. Ishigure, T., Horibe, A., Nihei, E., & Koike, Y. (1995). High-bandwidth, high-numerical aperture graded-index polymer optical fiber. Journal of lightwave technology, 13(8), 1686-1691.

15. Suar, M., Melchert, O., Rahlves, M., & Roth, B. (2019). Experimental and theoretical study of the formation process of photopolymer based self-written waveguides. Optics Express, 27(26), 38326-38336.

16. Suar, M., Baran, M., Günther, A., & Roth, B. (2020). Combined thermomechanical and optical simulations of planar-optical polymer waveguides. Journal of Optics, 22(12), 125801.

17. Brocklesby, W. S., Field, S. J., Hanna, D. C., Large, A. C., Lincoln, J. R., Shepherd, D. P., ... & Feng, X. (1992). Optically written waveguides in ion implanted Bi4Ge3O12. Optical Materials, 1(3), 177-184.

18. Frisken, S. J. (1993). Light-induced optical waveguide uptapers. Optics letters, 18(13), 1035-1037.

19. Sukhorukov, A. A., Shoji, S., Kivshar, Y. S., & Kawata, S. (2002). Self-written waveguides in photosensitive materials. Journal of Nonlinear Optical Physics & Materials, 11(04), 391-407.

20. Maruo, S., & Ikuta, K. (2000). Three-dimensional microfabrication by use of single-photon-absorbed polymerization. Applied Physics Letters, 76(19), 2656-2658.

21. Maruo, S., Nakamura, O., & Kawata, S. (1997). Three-dimensional microfabrication with two-photon-absorbed photopolymerization. Optics letters, 22(2), 132-134.

22. Shoji, S., & Kawata, S. (2000). Photofabrication of three-dimensional photonic crystals by multibeam laser interference into a photopolymerizable resin. Applied Physics Letters, 76(19), 2668-2670.

23. Kawata, S., Sun, H. B., Tanaka, T., & Takada, K. (2001). Finer features for functional microdevices. Nature, 412(6848), 697-698.

24. Cumpston, B. H., Ananthavel, S. P., Barlow, S., Dyer, D. L., Ehrlich, J. E., Erskine, L. L., ... & Qin, J. (1999). Two-photon polymerization initiators for three-dimensional optical data storage and microfabrication. Nature, 398(6722), 51-54.

25. Yamashita, T., Kagami, M., & Ito, H. (2002). Waveguide shape control and loss properties of light-induced self-written (LISW) optical waveguides. Journal of lightwave technology, 20(8), 1556.

26. Dorkenoo, K. D., Gillot, F., Crégut, O., Sonnefraud, Y., Fort, A., & Leblond, H. (2004). Control of the refractive index in photopolymerizable materials for (2+ 1) D solitary wave guide formation. Physical review letters, 93(14), 143905.

27. Saleh, B. E., & Teich, M. C. (2019). Fundamentals of photonics. john Wiley & sons.

28. Ishigure, T., Nihei, E., & Koike, Y. (1996). Optimum refractive-index profile of the graded-index polymer optical fiber, toward gigabit data links. Applied Optics, 35(12), 2048-2053.

29. Graded-index fibers calculation. (n.d.). Retrieved March 16, 2021, from https://www.fiberoptics4sale.com/blogs/optical-fibers-and-cables/100451910-graded-index-fibers-calculation

30. Frisken, S. J. (1993). Light-induced optical waveguide uptapers. Optics letters, 18(13), 1035-1037.

31. Sukhorukov, A. A., Shoji, S., Kivshar, Y. S., & Kawata, S. (2002). Self-written waveguides in photosensitive materials. Journal of Nonlinear Optical Physics & Materials, 11(04), 391-407.

32. Flory, P. J. (1953). Principles of polymer chemistry. Cornell University Press.

33. Odian, G. (2004). Principles of polymerization. John Wiley & Sons.

34. Kewitsch, A. S., & Yariv, A. (1996). Nonlinear optical properties of photoresists for projection lithography. Applied physics letters, 68(4), 455-457.

35. Monro, T. M., de Sterke, C. M., & Poladian, L. (1995). Self-writing a waveguide in glass using photosensitivity. Optics communications, 119(5-6), 523-526.

36. D. K. W. Lam and B. K. Garside, Appl. Optics 20, 440 (1981).

37. Hand D. P., & Russell, P. S. J. (1990). Photoinduced refractive-index changes in germanosilicate fibers. Optics letters, 15(2), 102-104.

38. de Sterke, C. M., An, S., & Sipe, J. E. (1991). Growth dynamics of phase gratings in optical fibers. Optics communications, 83(5-6), 315-321.

39. Lingnau, J., & Meyerhoff, G. (1984). The spontaneous polymerization of methyl methacrylate, 7. External heavy atom effect on the initiation. Die Makromolekulare Chemie: Macromolecular Chemistry and Physics, 185(3), 587-600.

40. Lingnau, J., & Meyerhoff, G. (1984). Spontaneous polymerization of methyl methacrylate. 8. Polymerization kinetics of acrylates containing chlorine atoms. Macromolecules, 17(4), 941-945.

41. Diemeer, M. B. (1998). Polymeric thermo-optic space switches for optical communications. Optical Materials, 9(1-4), 192-200.

42. Mueller, H. (1935). Theory of photoelasticity in amorphous solids. Physics, 6(6), 179-184.

43. Waxler, R. M., Horowitz, D., & Feldman, A. (1979). Optical and physical parameters of Plexiglas 55 and Lexan. Applied Optics, 18(1), 101-104.

44. Zhang, Z., Zhao, P., Lin, P., & Sun, F. (2006). Thermo-optic coefficients of polymers for optical waveguide applications. Polymer, 47(14), 4893-4896.

45. Stewart, W. J. (1977). A new technique for measuring the refractive index profiles of graded optical fibers. Tech. Dig. IOOC (IECE, Tokyo), 1977, 395-398.

46. Marcuse, D. (1972). Light transmission optics. New York, Cincinnati.

47. Marcuse, D., & Presby, H. M. (1980). Index profile measurements of fibers and their evaluation. Proceedings of the IEEE, 68(6), 666-688.

48. Jackson, J. D. (1999). Classical electrodynamics.

49. Born, M., & Wolf, E. (2013). Principles of optics: electromagnetic theory of propagation, interference and diffraction of light. Elsevier.

50. Yariv, A., Yeh, P., & Yariv, A. (2007). Photonics: optical electronics in modern communications (Vol. 6). New York: Oxford University Press.

51. Okoshi, T., & Kikuchi, K. (1988). Coherent optical fiber communications (Vol. 4). Springer Science & Business Media.

52. Kokubun, Y., & Iga, K. (1980). Mode analysis of graded-index optical fibers using a scalar wave equation including gradient-index terms and direct numerical integration. JOSA, 70(4), 388-394.

53. Hadley, G. R. (1992). Wide-angle beam propagation using Padé approximant operators. Optics Letters, 17(20), 1426-1428.

54. Hadley, G. R. (1992). Multistep method for wide-angle beam propagation. Optics Letters, 17(24), 1743-1745.

55. Kawano, K., & Kitoh, T. (2004). Introduction to optical waveguide analysis. Wiley-Interscience.

56. Yevick, D. (1994). A guide to electric field propagation techniques for guided-wave optics. Optical and Quantum Electronics, 26(3), S185-S197.

57. Schmidt, S. (2018). Efficient wave-optical simulations for the modeling of micro-optical elements (Doctoral dissertation).

58. Bi, Z. (2017). Finite Element Analysis Applications: A Systematic and Practical Approach. Academic Press.

59. Su, C., Cope, A., Ramsey, B., & Wong, K. (2014). Modeling the Effects of Increased Glucose Concentration on Intraocular Pressure.

60. Aronow R. et al. Multiple Scale Modeling for Predictive Material Deformation Analysis, Mathematics and Statistics Newsletter, University of Massachusetts Amherst, Volume 33, pp 4-6, 2017-2018

61. The Department of Civil Engineering at the University of Memphis CIVIL 7117 course notes

62. Department of Mathematics at Lamar University course notes.

63. Hysing, J. S. (2019, July 10). FEATool Multiphysics. Retrieved January 10, 2021, from https://www.featool.com/doc/physics.html

64. Appendix A: Thermophysical Properties. (2007, November 06). Retrieved January 11, 2021, from https://onlinelibrary.wiley.com/doi/pdf/10.1002/9780470172605.app1

65. Agarwal, S., Saxena, N. S., & Kumar, V. (2014). Temperature dependence thermal conductivity of ZnS/PMMA nanocomposite. In Physics of Semiconductor Devices (pp. 737-739). Springer, Cham.

66. Pavlinov, L. I., Rabinovich, I. B., Okladnov, N. A., & Arzhakov, S. A. (1967). Heat capacity of copolymers of methyl methacrylate with methacrylic acid in the region 25–190° C. Polymer Science USSR, 9(3), 539-544.

67. Keenan, JH, Chao, J., and Kaye, J., Gas Tables International Version, 2nd ed., John Wiley & Sons

68. Touloukin, Y. S. (1979). Thermophysical Properties of Matter, Vol. 3: Thermal Conductivity, Gasses. IFI/Plenum New York, 512.

69. Liu, G., & Quek, S. The finite element method.

70. SAFETY DATA SHEET. Retrieved from https://www.norlandprod.com /msds/SDS%20GHS/NOA%2068%20SDS%20GHS.pdf

71. Song, Y. J., & Peters, K. J. (2011). A self-repairing polymer waveguide sensor.

72. Ishigure, T., Horibe, A., Nihei, E., & Koike, Y. (1995). High-bandwidth, highnumerical aperture graded-index polymer optical fiber. Journal of lightwave technology, 13(8), 1686-1691.

73. van Gastel, M. H., Rosielle, P. N., & Steinbuch, M. (2019). A concept for accurate edge-coupled multi-fiber photonic interconnects. Journal of Lightwave Technology, 37(4), 1374-1380.

74. Malallah, R. E., Abdullah, A. Q., & Sheridan, J. T. (2020, April). Monitoring of photopolymerization induced changes of self-written waveguides. In Nonlinear Optics and its Applications 2020 (Vol. 11358, p. 113581U). International Society for Optics and Photonics.

APPENDICES

Appendix A: Structure of Polymer and the Types of Polymerization

Monomers are the building blocks of the polymers. These small molecules undergo polymerization process with the help of heat or light and they are combined to form bigger molecules which are called as polymers. A polymer molecule can be consisted of from 100 to tens of thousands or even more. Polymerization process is classified according to the polymer structure or polymerization process into condensation and addition or step and chain respectively. The condensation and step terms are used with the same meanings as well as addition and chain. Lately, the step and chain are preferred to be used for classification.

Appendix B: Numerical Modeling of the RIPs for the Heating and the Cooling

The MATLAB codes are written for the heating and the cooling processes, respectively:

```
figure(1);
g1=zeros(1,8);
ncore1=[1.5184495, 1.5182617, 1.5181906, 1.5180809, 1.5180035, 1.5178605,
1.5177671, 1.5176731];
ncladding1=[1.5176713, 1.5171087, 1.5169014, 1.5167392, 1.5165480, 1.5163251,
1.5161155, 1.5159058];
delta1=[0.000128140536077304, 0.000189891338610614, 0.000212337272301325,
0.000221002152147015, 0.000239763785110017, 0.000252952837572179,
0.000272118422042160, 0.000291204804935064];
y=zeros(8,50001);
for i=1:8
    g1(1,i)=2-(12/5*delta1(1,i));
end
disp(g1)
x=0:0.001:50;
for r=1:8
   y(r,:)=sqrt((1-2*delta1(1,r)*(x/25).^g1(1,r))*ncore1(1,r).^2);
       y(r,25001:50001)= ncladding1(1,r);
     plot(x,y(r,:));
     hold on
     plot(-x,y(r,:))
  hold on
end
xlim([-50 50])
xlabel('R [\mum]') ;
ylabel('Refractive Index [n(r)]') ;
```

```
figure(2);
g2=zeros(1,8);
ncore2=[1.5185111183, 1.5183084140, 1.5182316710, 1.5181132650, 1.5180297220,
1.5178753730, 1.5177745000, 1.5176731000];
ncladding2=[1.517810318, 1.517108700, 1.516901400, 1.516739200, 1.516548000,
1.516325100, 1.516115500, 1.515905800];
delta2=[0.000115389536156003, 0.000197580260305431, 0.000219097412506402,
0.000226329631278721, 0.000244080159590773, 0.000255401245449466,
0.000273336650056616, 0.000291204804935064];
y=zeros(8,50001);
for i=1:8
     g2(1,i)=2-(12/5*delta2(1,i));
end
disp(g2)
x=0:0.001:50;
for r=1:8
    y(r,:)=sqrt((1-2*delta2(1,r)*(x/25).^g2(1,r))*ncore2(1,r).^2);
         y(r,25001:50001)= ncladding2(1,r);
      plot(x,y(r,:));
      hold on
      plot(-x,y(r,:))
   hold on
end
xlim([-50 50])
```